Order Number 8724576

Slow collisions of H^- and D^- with Na, K and Cs

Wang, Yicheng, Ph.D.

The College of William and Mary, 1987

U·M·I
300 N. Zeeb Rd.
Ann Arbor, MI 48106

Slow Collisions of H^- and D^- with Na, K and Cs

A Dissertation

Presented to

The Faculty of the Department of Physics

The College of William and Mary in Virginia

In Partial Fulfillment

Of the Requirement for the Degree of

Doctor of Philosophy

by

Yicheng Wang

1987

APPROVAL SHEET

This dissertation is submitted in partial fulfillment

of the requirement for the degree of

Doctor of Philosophy

Yicheng Wang

Approved, May 1987

Roy L. Champion

Lynn D. Doverspike

John B. Delos

Morton Eckhause

Stephen K. Knudson,
Department of Chemistry

CONTENTS

ACKNOWLEDGMENTS

I wish to thank my advisors Roy Champion and Lynn Doverspike for their guidance, patience and trust. I am also indebted to John Delos, Morton Eckhause, Steve Knudson and Jean Pierre Gauyacq for their careful reading of the manuscript and their helpful suggestions.

Michael Huels is accredited for Fig.4.1.

ABSTRACT

The cross sections of charge transfer and electron detachment in collisions of H^- and D^- with Na, K and Cs have been measured for collision energies ranging from 3 to 300 eV. Both charge transfer and electron detachment are significant electron-loss mechanisms for $H^-(D^-)$; both processes exhibit velocity-dependent isotope effects for $H^-$and D^-. $\sigma_{ct}(E)$ displays high energetic thresholds for Na and K (about 20 eV for H^- + Na and 40 eV for H^- + K) yet no obvious one for Cs. $\sigma_e(E)$ does not depend on the target as much as $\sigma_{ct}(E)$ and displays near zero-energy thresholds. The relative importance of charge transfer as an electron-loss mechanism decreases as the mass of the alkali-metal increases.

Slow Collisions of H^- and D^- with Na, K and Cs

INTRODUCTION

This study of slow collisions involving hydrogen negative ions and alkali-metal atoms is a continuation of research in the Atomic and Molecular Collision Laboratory at the College of William and Mary. The collisional systems which have been previously studied in this laboratory include the negative ions of atoms such as hydrogen, oxygen, alkali-metals and halogens with rare gases and selected molecular gases. The total cross sections for electron detachment, charge transfer and reactive scattering in these collisions have been measured with a beam-target-gas apparatus.[1] In that apparatus, an ion beam with well-defined energy passes through a static gas target; electrons and slow negative ions produced in collisions are trapped and separated by combined electric and magnetic fields. Molecular targets which can be studied with that apparatus are numerous. Atomic targets, however, are limited to rare gases since they are the only elements which exist in natural atomic form at room temperature.

Collisions of negative ions with chemically more reactive atoms are interesting. A prototype of such a collision is H^- + Na. Since both H and Na are attractive sources for the "extra" electron, the quasi-molecular ion NaH^- has two bound states, which go to H^- + Na and H + Na^- in the separated atom limit; both states have very diffuse electron clouds. For the charge transfer reaction

$$H^- + Na \rightarrow H + Na^-,$$

the initial and final states have an energy gap of only 0.2 eV. This asymptotic near-degeneracy mediates the transitions between these two states.

In addition to the above particular reaction of charge transfer at large internuclear separation, electron detachment may happen in H^- + Na collisions at small internuclear separation as for the H^- + rare-gas systems[2]. When H^- comes sufficiently close to Na, NaH^- becomes unstable and may decay by emitting an electron,

$$H^- + Na \rightarrow H + Na + e.$$

The work reported in this thesis describes the detailed studies of these two competing electron-loss channels for H^- in collisions with several alkali-metal (gas-phase) targets.

A crossed-beam apparatus has been built in this laboratory to measure cross sections for charge transfer and electron detachment in collisions of negative ions with various atoms. This apparatus will be described in detail in chapter 2. Briefly, an ion beam with well-defined energy is crossed with an atomic target beam. The electrons and charge transfer products produced in collisions are extracted electrically and separated magnetically. The first experiment with this new apparatus was to study collisions of H^-, the simplest negative ion, with selected alkali-metals, Na, K and Cs, which are the easiest to prepare when compared with other atoms except rare gases.

The experimental results for collisions of H^- with Na, K and Cs will be presented and discussed in chapter 3; they were originally reported in two publications:

1) Yicheng Wang, R. L. Champion and L. D. Doverspike, Phys. Rev. A 35, 1503 (1987).
2) Yicheng Wang, R. L. Champion and L. D. Doverspike, Phys. Rev. A 36, 381 (1987).

Chapter 1

BASICS OF NEGATIVE IONS

This chapter first reviews the elementary knowledge concerning the stability, formation and destruction of negative ions, then surveys several theoretical models for electron detachment in negative ion collisions, and concludes with a discussion of a semi-classical approximation for atomic collisions.

1.1. Stability of Negative Ions

The stability of a neutral atom is clear; the Coulomb force holds the electrons and the nucleus together. But how can a electrically neutral atom hold an "extra" electron and thus form a negative ion? What is the force between them?

When an atom is exposed to the electric field of a free electron, the atom undergoes polarization; the nucleus tends to be attracted while the atomic electrons are repelled by the free electron. Such a polarized atom forms its own dipole electric field and, as a result, attracts the free electron. It follows from this argument that a free electron will feel an attractive potential surrounding any atom.

However, not every three-dimensional potential possesses a bound state. For example, a particle of mass m in rectangular well

$$V = \begin{cases} -V_o & (r < r_o) \\ 0 & (r \geq r_o) \end{cases}$$

contains no discrete energy level unless $V_o r_o^2 > \pi^2\hbar^2/8m$ (Ref.3). The induced dipole interaction between a free electron and an atom is not solely responsible for the stability of a negative ion, because the Pauli principle which excludes two electrons from occupying the same quantum state limits the polarization interaction.[4]

In addition to the static attractive field due to polarization of the atom, another cause which plays a vital role in the stability of a negative ion is the exchange correlation effects between the attached and atomic electrons. This exchange correlation is a pure quantum effect and, like any other quantum effect, can only be explained with wave functions which have no classically tangible meaning. To illustrate this point, let us consider the negative ion of hydrogen.

The calculation of the electron affinity (which is defined as the difference between the total energies of the neutral atom and the corresponding negative ion) of this simplest ion, H^-, involves the solution of a two-body problem analogous to that of the helium atom. An exact solution is not possible but variational methods may be used to obtain very accurate values for the electron affinity. For simplicity, we will use trial functions which have only one adjustable parameter. We will compare the result obtained for the total energy of the system, using a trial wave function (in atomic units)

$$\phi(r_1,r_2) = \exp(-r_1-\alpha r_2)$$

which includes no correlation, with the result using

$$\begin{aligned}\Psi(r_1,r_2) &= \exp(-r_1-\alpha r_2) + \exp(-r_2-\alpha r_1)\\ &= \phi(r_1,r_2) + \phi(r_2,r_1)\end{aligned}$$

which includes correlation.

Detailed formulas are given in Appendix A. The trial function ϕ yields the total energy of H^-

$$E(\alpha) = -\frac{1}{2} + \frac{\alpha^2}{2} - \frac{\alpha^3(2+\alpha)}{(1+\alpha)^3}$$

which has a minimum at $\alpha = 0$ and

$$E_{min} = -1/2 \quad \text{(hartree)} .$$

This minimum energy equals the ground energy of a neutral hydrogen atom. Thus the trial function ϕ fails to predict the stability of H^-.

For the trial function Ψ, the total energy of H^- is given by

$$E(\alpha) = -\frac{(1-\alpha)(1+\alpha)^7 + 2\alpha^3(2+\alpha)(1+\alpha)^3 + 8\alpha^3(11-5\alpha)}{2(1+\alpha)^6 + 128\alpha^3} .$$

Its minimum is numerically found at about $\alpha = 0.28$ and

$$E_{min} \approx -0.513 \quad \text{(hartree)}.$$

This minimum energy is less than the bound energy of the ground hydrogen atom; thus the trial wavefunction Ψ which includes the exchange correlation predicts the stability of H^-.

We use the above simple trial wavefunction Ψ to illustrate the importance of correlation effects in leading to the stable negative ion. This wavefunction may still deviate significantly from reality. By increasing the number of adjustable parameters in the trial wavefunction, accuracy of variational methods can be increased. Hart and Herzberg[5] used a trial wavefunction with 20 adjustable parameters for H^- and found the electron affinity to be 0.75421 eV, which agrees extremely well with one of the best experimental determinations, 0.7539 eV, obtained by Feldmann[6] using the photodetachment method.

The electron affinities of other atoms can be calculated, in principle, in the same way. However the electron affinity is the very small difference between the total energy of the parent atom and the corresponding negative ion, and it is not possible as yet to calculate it to any desired precision for any atom other than hydrogen. The electron affinities of most known negative ions are obtained experimentally, e.g., by observing the thresholds of the photodetachment of the negative ions. The electron affinities of selected elements are listed Table 1.1.

1.2. Formation and Destruction of Negative Ions

Most of the elements in the periodic table, including the most electro-negative halogens on one end and the most electro-positive alkali-metals on the other, can form stable negative ions.

The simplest manner in which negative ions can be formed is the direct capture of a free electron by a neutral atom

$$A + e \rightarrow A^- + \Delta E$$

where ΔE is the kinetic energy of the electron before the encounter plus the electron affinity of the atom. An amount of energy ΔE is released by the capture and must be dissipated in some way. This may occur by radiation or by transmission of the surplus energy to a third body.

Another possibility to produce negative ions is dissociative attachment, for example

$$e + H_2 \rightarrow H_2^{-*} \rightarrow H^- + H$$

TABLE 1.1

Electron Affinities of Selected Elements

Element	Electron affinity (eV)	Reference
H	0.7539±0.0002	(6)
Li	0.620±0.007	(7)
Na	0.548±0.004	(7)
K	0.50147±0.0001	(8)
Rb	0.4860±0.005	(7)
Cs	0.4715±0.0003	(9)
C	1.2629±0.0003	(10)
N	< 0	(11)
O	1.465±0.005	(12)
F	3.400±0.002	(13)
Cl	3.613±0.002	(14)
Br	3.366±0.002	(13)
I	3.063±0.003	(15)

in which an electron collides with and is captured by H_2. H_2^{-*} then dissociates into H^- + H (Ref.16). Energy released on capture in this process appears as vibrational excitation of the molecular ion, which subsequently appears as kinetic energy of the nuclei following dissociation.

The inverse reaction of every process of negative-ion formation leads to the destruction of negative ions. Reactions which involve negative-ion formation and destruction occur wherever atoms, molecules and free electrons are present, such as in glow discharges, flames, gas-laser medium, the ionosphere of the earth and the photospheres of the sun and stars.

For example, H^- largely determines the spectral distribution of the continuous solar emission in the observable wavelength region. The solar spectrum is produced by a black body radiator but modified by absorption of the solar photosphere. The black body radiation is universally described by the Planck's law while the absorption depends on the absorbing constituents. Experimental results indicate that there is strong absorption by the solar photosphere at wavelengths > 5000 Å. The chief constituent of the sun is hydrogen but, in order to explain the strong absorption at the long wavelengths, it appeared necessary to suppose that atoms with low ionization potential, such as those of metal, were present in sufficient proportion to provide the absorption. Grave difficulties were, however, associated with this interpretation. The main one concerned the strength of the metallic absorption lines. If metals were present in sufficient quantities to provide the observed continuous absorption they would produce much stronger absorption lines than were observed. Furthermore, they would give rise to a number of absorption edges which are not found.[17] The way out of this difficulty was first shown by Wildt.[18] He pointed out that, at the temperatures and electron pressure prevalent in the sun, a portion of the atomic hydrogen would be present as negative ions which have a low threshold for continuous absorption. Detailed experiments and calculations carried out later confirmed this hypothesis.[4,17]

As another example which is more closely related to the work described in this dissertation, cesium-metal vapor is often employed in H^- ion sources of the plasma-discharge type to enhance the efficiency of H^- production.[19] Although H^- ions appear to be primarily produced on cesium-metal-coated surfaces in such an ion source, the process $H^- + Cs \rightarrow H + \ldots$ in the gas phase is one of the reactions leading to the destruction of H^- and thus determines the intensity of H^- that can be realized. Such intense H^- beam sources are of very practical concern. H^- ion beams are used to heat fusion plasmas such as in

Tokamaks. The ions, after being accelerated, need to be neutralized to penetrate the strong magnetic field containing the plasma. H^- is "flimsy" and easier to neutralize than H^+.

1.3. Models for Slow Collisions of Negative Ions

Since an exact solution to the Schrödinger equation of a collisional system involving a negative ion and an atom is impossible, some models have been developed to describe such collisions. The systems which have been studied extensively, both theoretically and experimentally, at low collision energy are

$$H^- + R \rightarrow H + R + e$$

where R stands for rare gas atoms. One of the obvious differences between systems involving rare gas targets and alkali-metal targets is that electron detachment is the only electron loss channel for H^- with the former while both electron detachment and charge transfer can play roles in the latter. Thus, a greater degree of complexity is expected for collisions of H^- with alkali-metal atoms. Nevertheless, it is beneficial to review the existing models for $H^- + R$ systems.

Electron detachment was first described by a curve-crossing model,[20] in which it was assumed that the potential curve of the discrete bound state of the negative ion crossed into the continuum states representing the neutral molecule and a free electron, the discrete state becoming a resonance. This resonance or quasibound state is assumed to decay with a half-life inversely proportional to $\Gamma(R)$. In the description of this model, the electron detachment probability of the negative ion is given by

$$P(b) = \exp[-2\int_{R_0}^{\infty} dR\ \Gamma(R)/v]$$

This model predicts that if we compare collisions involving H^- with those involving D^- at the same relative collision energy, the heavier, slower isotope will have a larger cross section for electron detachment. This isotope effect is seen in collisions of H^- and D^- with He (Ref. 20), and in that case the model is in quantitative agreement with low-energy experiments. A configuration-interaction (CI) calculation of the potential curves for the ground states of HeH^- and HeH carried out later does indeed show that the HeH^- molecular state clearly crosses the HeH continuum.[21]

The curve-crossing model encountered difficulty in the case of collisions of H^- and D^- with Ne. CI calculations of the ground potential curves of NeH^- and NeH indicate that the curve of NeH^- merges with that of NeH without an obvious crossing.[21] An isotope effect opposite to that predicted by the curve-crossing model is observed[2] in this case and suggests that a different model of electron detachment is required for these systems.

Using a zero-range-potential (ZRP) model, Gauyacq[22,23] explained the inverse isotope effect which was observed in the $H^-(D^-)$ + Ne collisions. In the ZRP model, detachment may occur when the binding energy $\epsilon(R)$ for the outer electron (taken to be the energy gap between the ionic and the neutral states as a function of the internuclear separation R) becomes small during collision. For small values of $\epsilon(R)$, the wavefunction of the outer electron is extremely diffuse and the electronic motion is slow. Consequently, the outer electron can only imperfectly adjust to the changing molecular field during the collision and detachment becomes possible. Since the size of the molecular core is much smaller than the dimension of the active electronic wavefunction, the electron detachment problem is mathematically addressed by assuming that the outer electron is bound to the molecular core by a time-dependent potential well of very short range. The electronic wavefunction outside the well satisfies the free-particle Schrödinger equation subject to a time-dependent boundary condition

$$\left. \frac{1}{r\psi} \frac{\partial (r\psi)}{\partial r} \right|_{r \to o} = f[R(t)] \tag{1.1}$$

f(R) contains all the information about the molecular core, and determines all the characteristics exhibited by differential as well as total cross sections.

In the region of R where the quasi-molecular ion is bound, it can be assumed that, to the first order,

$$f(R) = - [2\epsilon(R)]^{1/2} \qquad (1.2)$$

since the electronic wavefunction outside the well has the form of $\exp(-kr)/r$ with $k = [2\epsilon(R)]^{1/2}$, when R is held fixed. In the region where the ionic state is not bound, f(R) is not so easy to obtain and has been extrapolated linearly from equation (1.2) in practice.[22,23] With $f[R(t)]$ known, the free-particle Schrödinger equation, subject to the time-dependent boundary condition (1.1), can then be solved numerically and projected onto the bound eigenfunction at $t = \infty$ in order to determine the survival and detaching probabilities.

A different approach to the theory of electron detachment was developed by Taylor and Delos.[24,25] They expanded the wave function of the active electron in an orthogonal representation of electronic states and obtain a set of coupled equations. They assumed the coupling function between the ionic and continuum states in a exponential form with two adjustable parameters, and solved the coupled equations for both $H^-(D^-)$ + He (Ref. 25) and $H^-(D^-)$ + Ne (Ref. 26) collisions, and obtained good agreement with the experimental results. Their approach is very general, and is closely related to the semi-classical two-state approximation for electronic transitions which will be described in the following section.

1.4. Semi-classical Description of Atomic Collisions

Rigorously, both electronic and nuclear degrees of freedom in atomic collisions should be described by quantum mechanics; since the full Hamiltonian of a collision system is time independent, the system obeys the full stationary Schrödinger equation

$$H(R,r)\ \Psi(R,r) = E\ \Psi(R,r)$$

subject to the usual scattering boundary condition. The Hamiltonian is

$$H(R,r) = -\frac{\hbar^2}{2\mu}\nabla_R^2 + h(r,R)$$

where, for a one-electron system,

$$h(r,R) = -\frac{\hbar^2}{2m}\nabla_r^2 + V(r,R) + h_{soc}$$

with $V(r,R)$ being the total potential energy of interaction of the electron and both nuclei, and h_{soc} being the "magnetic" Hamiltonian, which includes spin-orbit coupling and other smaller magnetic effects. In principle, this equation can be solved numerically, by beginning with the expansion of the wave function Ψ in a discrete basis that spans the electronic space and thus yields "close coupled" equations for the nuclear wave function.[27]

A much simpler description of atomic collisions is, however, obtained if the nuclei are assumed to move classically along some path. In fact, this assumption is often justified even in slow collisions because the nuclei involved have much shorter de Broglie wavelength than the electrons surrounding them. For example, at 13.6 eV collision energy, the proton in H^- ion has a de Broglie wavelength $(M_p/m_e)^{\frac{1}{2}} \approx 43$ times shorter than the electron in a hydrogen atom. The wave behavior of the nuclei is negligible in comparison to the electronic motion; the motion of the nuclei can thus be treated classically. The electrons then feel an intrinsically time-dependent force field because of the motion of the nuclei; the electronic wave function $T(\mathbf{r},t)$ must satisfy a time-dependent Schrödinger equation with the Hamiltonian being $h[\mathbf{r},R(t)]$.

The "magnetic" Hamiltonian, h_{soc}, can be further neglected since it is much smaller than the "electric" Hamiltonian as in the hydrogen atom where the magnetic energy is a fraction, about α^2 (α is the fine structure constant), of the electric energy. Under these circumstances, the electronic Hamiltonian is called the Born-Oppenheimer Hamiltonian

$$h(\mathbf{r},R) = -\frac{\hbar^2}{2m}\nabla_{\mathbf{r}}^2 + V(\mathbf{r},R)$$

and the Schrödinger equation is

$$i\hbar \frac{\partial}{\partial t} T(r,t) = h[r,R(t)]\ T(r,t)$$

To solve the above equation, we expand T in a complete and orthogonal basis $\{\phi_n(r,R)\}$

$$T = \sum_n C_n(t)\ \phi_n[r,R(t)]$$

and we have

$$i\hbar \frac{d}{dt} \underline{C} = (\underline{h} + v \cdot \underline{P})\ \underline{C} \qquad (1.3)$$

where v is the relative nuclear velocity dR/dt, and

$$h_{mn} = \langle \phi_m | h | \phi_n \rangle$$

$$P_{mn} = \langle \phi_m | -i\hbar \nabla_R | \phi_n \rangle$$

If the basis $\{\phi_n\}$ is the set of eigenfunctions of the Born-Oppenheimer Hamiltonian with the nuclei held fixed

$$h(r,R)\ \phi_n(r,R) = \epsilon_n(R)\ \phi_n(r,R),$$

then the matrix $\underline{h}$ in equation (1.3) is diagonal and the basis $\{\phi_n\}$ is called the adiabatic representation. In the adiabatic representation, the "non-adiabatic" coupling matrix $v \cdot \underline{P}$ causes transitions between states.

Another representation often used in practice is one in which the coupling matrix $v \cdot \underline{P}$ vanishes or is negligibly small; it is called the diabatic representation. The $\underline{h}$ matrix is usually not diagonal in this representation and its off-diagonal elements cause transitions between states.

Since both the adiabatic $\{\phi_n^a\}$ and diabatic $\{\phi_n^d\}$ bases are supposed to be complete and orthogonal, there is an unitary matrix $\underline{U}$ relating these two bases,

$$\underline{\phi}^a = \underline{\phi}^d \, \underline{U},$$

and their Hamiltonian matrixes,

$$\underline{U}^\dagger \, \underline{h}^d \, \underline{U} = \underline{h}^a .$$

From equation (1.3), we also have

$$(v \cdot \underline{P})^a = \underline{U}^\dagger \, (v \cdot \underline{P})^d \, \underline{U} - i\hbar \, \underline{U}^\dagger \, \frac{d}{dt} \, \underline{U}$$

For a given problem, either the adiabatic or diabatic representations can be used, and they should give the same answer. However one representation may be more suitable to the problem than the other. To expand on this point, let us take a two-state problem as an example.

Suppose we know that the Hamiltonian matrix in a diabatic representation is $\underline{h}^d$, then the unitary matrix given by

$$\underline{U} = \begin{pmatrix} \cos\omega & \sin\omega \\ -\sin\omega & \cos\omega \end{pmatrix}$$

with

$$tg2\omega = \frac{2h_{12}^d}{h_{22}^d - h_{11}^d} ,$$

diagonalizes $\underline{h}^d$ and is the unitary matrix relating the diabatic representation to the adiabatic representation. Thus, in the adiabatic representation, we have

$$h_{nn}^a = (h_{11}^d + h_{22}^d)/2 \pm [(h_{22}^d - h_{11}^d)^2/4 + (h_{12}^d)^2]^{½}$$

or

$$(h_{22}^a - h_{11}^a)^2 = (h_{22}^d - h_{11}^d)^2 + 4(h_{12}^d)^2$$

and

$$(v\cdot\underline{P})^a = i\hbar \frac{d\omega}{dt} \begin{pmatrix} 0 & -1 \\ 1 & 0 \end{pmatrix}$$

or

$$(v\cdot\underline{P})_{12}^a = -i\hbar v_R \frac{d\omega}{dR} \tag{1.4}$$

$$= i\hbar v_R \frac{h_{12}^d \frac{d\Delta}{dR} - \Delta\frac{d}{dR}h_{12}^d}{\Delta^2 + 4(h_{12}^d)^2}$$

where

$$\Delta = h_{22}^d - h_{11}^d .$$

Since the coupling terms are known, evolution of the amplitude on each state can be obtained from equation (1.3) in either representation. Using the phase transformation

$$C_n(t) = B_n(t) \exp(i\theta_n)$$

with

$$\theta_n(t) = - \int_{-\infty}^{t} \frac{h_{nn}}{\hbar} dt',$$

we have

$$B_1^d(t) = \frac{1}{i\hbar} \int_{-\infty}^{t} B_2^d \; h_{12}^d \; \exp[i(\theta_2^d - \theta_1^d)] \; dt'$$

$$B_2^d(t) = \frac{1}{i\hbar} \int_{-\infty}^{t} B_1^d \; h_{12}^d \; \exp[i(\theta_1^d - \theta_2^d)] \; dt'$$

in the diabatic representation, and

$$B_1^a(t) = - \int_{-\infty}^{t} B_2^a \; v_R \; \frac{d\omega}{dR} \; \exp[i(\theta_2^a - \theta_1^a)] \; dt'$$

$$B_2^a(t) = \int_{-\infty}^{t} B_1^a \; v_R \; \frac{d\omega}{dR} \; \exp[i(\theta_1^a - \theta_2^a)] \; dt'$$

in the adiabatic representation.

When the collision is extremely slow, the transitions tend to zero in the adiabatic representation, reflecting the reality that the electrons have time to adjust continuously to the changing molecular field. However, transitions still occur in the diabatic representation. This becomes clear when one focuses on the transformation matrix: if the amplitudes are $C_1 = 1$ and $C_2 = 0$ in the adiabatic representation, they are $C_1 = \cos\omega$ and $C_2 = -\sin\omega$ in the diabatic representation. Thus, the adiabatic representation is the natural choice in very slow collisions.

In some cases, however, the diabatic representation has distinct advantages. For example, it would be advantageous in the curve-crossing problem where the diabatic potentials cross while the adiabatic potentials avoid crossing. In the adiabatic representation, the coupling increases abruptly and is strong near the crossing; consequently, the transitions are large. In the diabatic representation, on the other hand, the coupling changes smoothly and is weak near the crossing, this leading to small transition amplitudes. In other words, the system is more likely to follow the diabatic potentials in this case.

Chapter 2

EXPERIMENTAL APPARATUS AND METHODS

The apparatus used for this research is of the crossed-beam type. A schematic diagram which illustrates the main features of the apparatus is given in Fig.2.1. H^- and D^- ion beams extracted from the ion source are focused electrostatically and mass-selected with a Wien filter; the ion beam is then focused into the collision region.

The collision region is within a one-sixth section of a 127° cylindrical electrostatic energy analyzer. The voltage across the two curved plates of the analyzer allows the ion beam to pass resonantly through the analyzer section. The primary ion beam transmitted through the analyzer section is monitored with a Faraday cup-electrometer combination. The grid above the cup serves to determine the energy and energy spread of the ion beam, which is less than 5% of the transmission energy for all measurements reported here. It also serves to suppress any secondary electrons produced in collisions of the ion beam with the Faraday cup. The ion beam intersects, midway of its path inside the analyzer, with a neutral target beam. The electric field maintained across

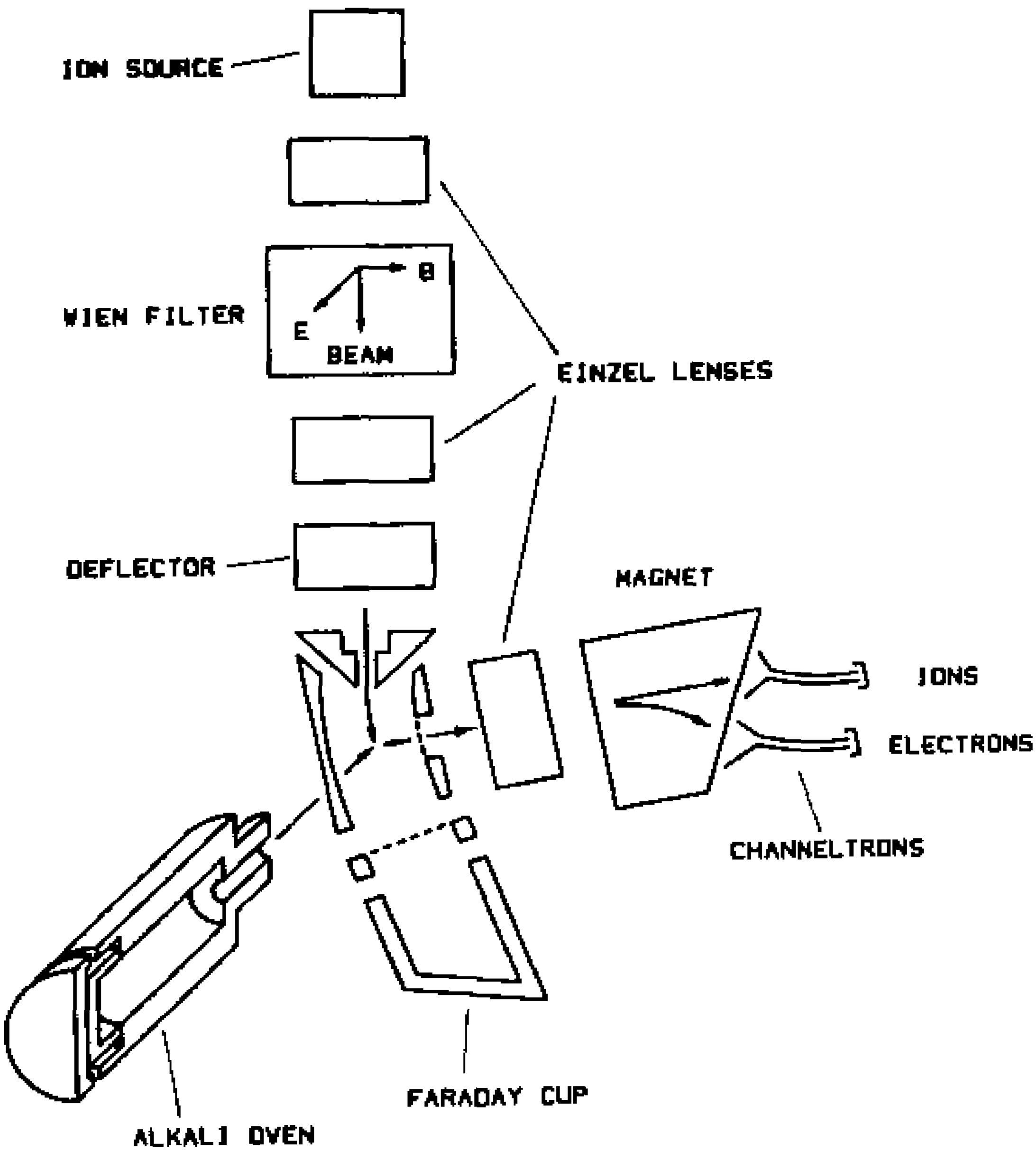

Fig.2.1. Schematic diagram of crossed-beam apparatus.

the analyzer is used to extract the slow anions and electrons produced in the collision region through a grid on the inner plate. The extracted anions and electrons are then focused with an Einzel lens, separated by a magnetic field and detected with conventional electron-multipliers.

The oven, together with a separate gas nozzle, is mounted on a platform whose rotational position is determined by a worm-gear-motor configuration precisely controlled by electronic sensors. The gas nozzle is identical in shape to the oven's exit cylinder and is used to direct a neutral beam of, e.g., Ar or O_2 into the collision region. This design enables one to monitor and calibrate the apparatus, before and during experiments with alkali vapors, using some previously studied reactants such as $H^- + O_2$ (Ref. 28) and $H^- + Ar$ (Ref. 1). Liquid-nitrogen-cooled surfaces are positioned to trap the undesired alkali vapor.

The full overlap of the ion beam with the target beam is assured since the target beam has approximately twice the diameter of the ion beam. This overlap is confirmed by the fact that a certain voltage change across the analyzer induces a negligible flux change of the product anions and electrons. The target thickness is chosen such that the attenuation of the ion beam is less than 5%, thus assuring that secondary collisions are negligible.

The relative collection efficiencies for different collision energies for each product are determined by normalization to the known cross sections of electron detachment, $\sigma_e(E)$, and charge transfer, $\sigma_{ct}(E)$, for $H^- + O_2$ (Ref. 28). These two cross sections are comparable in magnitude over the energy range of interest. The normalization procedure yields energy-dependent transmission functions for the product anion and electron collecting systems. A typical set of these functions (which were used for $H^-(D^-) + K$) are shown in Fig.2.2. The transmission function for anions is different from that for electrons mainly because of the different effects of the magnetic field. For reasons that will be discussed below, the transmission functions cannot be ascertained by using O_2 as the target gas while the alkali oven is hot. However, the transmission function for electron collection may be confirmed with $H^- + Ar$ (with the argon gas passing through a U-shaped liquid-nitrogen-cooled tube) during experiments involving alkali vapor.

In the following sections, we will describe in detail the hydrogen negative ion source, the alkali-metal atomic source, treatment of noise and data-acquisition procedures. We will also estimate the experimental errors associated with the data obtained.

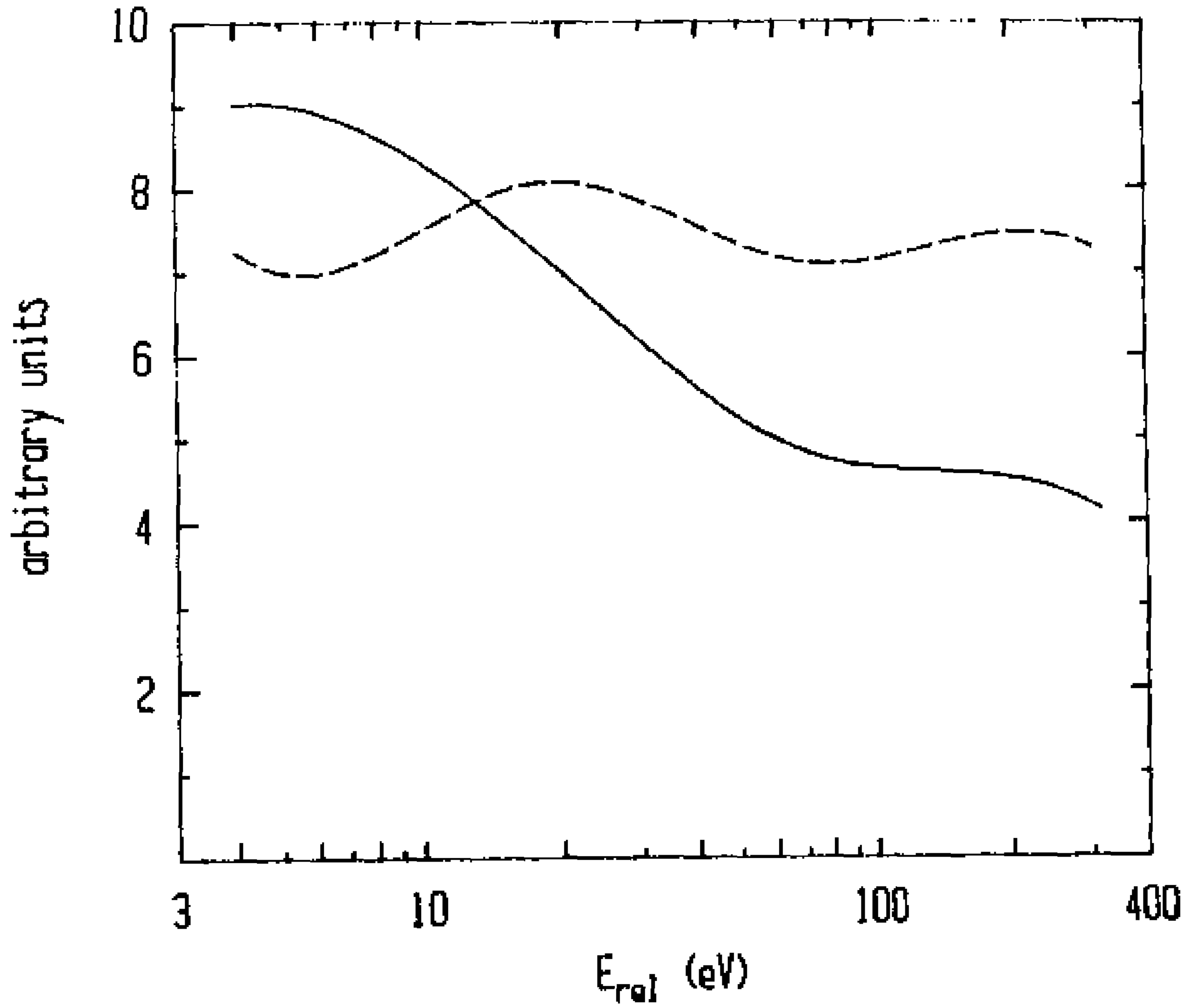

Fig.2.2. Calibration curves used for $H^-(D^-)$ + K. Solid line for ions; dashed line for electrons.

2.1. Hydrogen Negative Ion Source

The ion source used is an arc-discharge type. The arc is maintained inside a stainless steel chamber between the tip of a V-shaped 0.01" tungsten filament and the center region of the anode plate, which forms one end of the chamber. The gap between the tip of the filament and the anode plate is about 0.05". A source gas mixture of about 50% argon, 25% hydrogen and 25% deuterium is admitted into the chamber through a precision leak valve; the pressure in the chamber is maintained at about 0.1 Torr. Energetic electrons necessary to sustain the arc discharge are produced by heating the filament with about 12 amperes while applying -50 volts between the filament and the anode. About 50 mA arc current is usually observed between the filament and the anode.

The dynamics of negative ions in the arc is complicated because the mean free path in the chamber is about 0.1 mm. Nevertheless, the primary mechanism leading to negative ion formation is believed to be dissociative attachment,

$$e + H_2 \rightarrow H^- + H.$$

This is a well-studied process.[16] Two peaks are observed in total cross section measurement of dissociative attachment at about 4 and 14 eV of the electron energy with the cross sections of about 0.00006 and 0.0012 a_0^2, respectively. The first peak is associated with

$$e + H_2 \rightarrow H_2^-(^2\Sigma_u^+) \rightarrow H^- + H$$

and the second is with

$$e + H_2 \rightarrow H_2^-(^2\Sigma_g^+) \rightarrow H^- + H$$

The negative ions are extracted from the source chamber through a 0.02" diameter aperture located at the center of the anode plate. Since the mean free path in the source chamber is about one-fifth of the diameter of the aperture, only negative ions produced near the aperture have a significant chance of being extracted. The tip of the filament has been deliberately set off-center by about 1 mm to reduce the voltage drop near the aperture. Thus, the extracted negative ions have near-zero potential energy with respect to the anode; this is confirmed by energy analysis of the ion beams.

2.2. Alkali-metal Atom Source

The alkali-metal atoms are produced by heating the parent metal in an oven. The melting temperatures of sodium, potassium and cesium metals are 98, 64 and 29 ^oC, respectively. After melting, the alkali-metal liquid evaporates and eventually saturates the vapor. The saturation vapor pressures of the alkali metals are shown in Fig.2.3 as functions of the temperature of the oven.

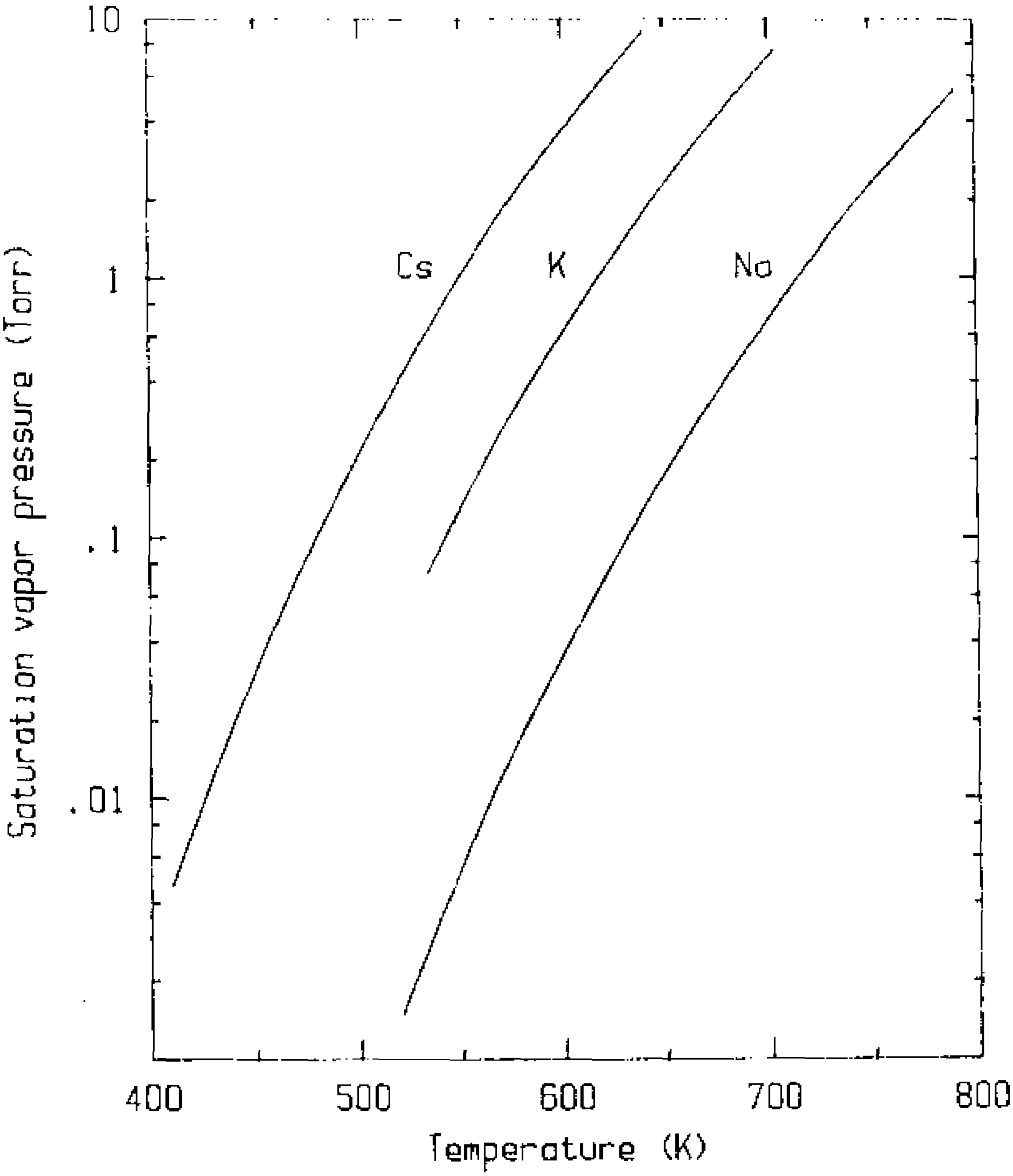

Fig.2.3. Saturation vapor pressure for Na, K and Cs. Their analytical formulas are $\ln(p) = 17.39 - 12423/T$ for Na, $\ln(p) = 16.54 - 10210/T$ for K (from Ref. 29), and $\ln(p) = 25.451 - 1.35\ln(T) - 9304.7/T$ (from Ref.30).

The dimer fraction in the vapor is estimated in Appendix B by assuming chemical equilibrium

$$2Na = Na_2$$

and the results are plotted in Fig.2.4.

The alkali oven is made of stainless steel and sealed with a removable cap made of Monel alloy. The oven is heated by iron-constantan thermocouple wire[31] wrapped around the grooved outside surface. The exit cylinder of the oven is densely wrapped with additional heating wire so that it can be maintained hotter than the main body of the oven; this prevents clogging of the exit orifice and reduces the dimer fraction in the atomic beam. A thermocouple attached to the oven monitors its temperature and also provides the feedback signal for regulation of the current to the heating wire in order to maintain the oven at a preset temperature. Typical operating temperatures of the oven are 350 ^{o}C for Na, 180 ^{o}C for K and 200 ^{o}C for Cs. The dimer concentration in the beam in each case is negligible, which is evidenced by comparing data obtained at different oven temperatures.

Loading of the alkali metals into vacuum chamber is worth mentioning. Sodium and potassium used in the experiments come from the manufacturer in lumps immersed in oil. A small piece of fresh-cut alkali metal is therefore washed in petroleum ether before loading into

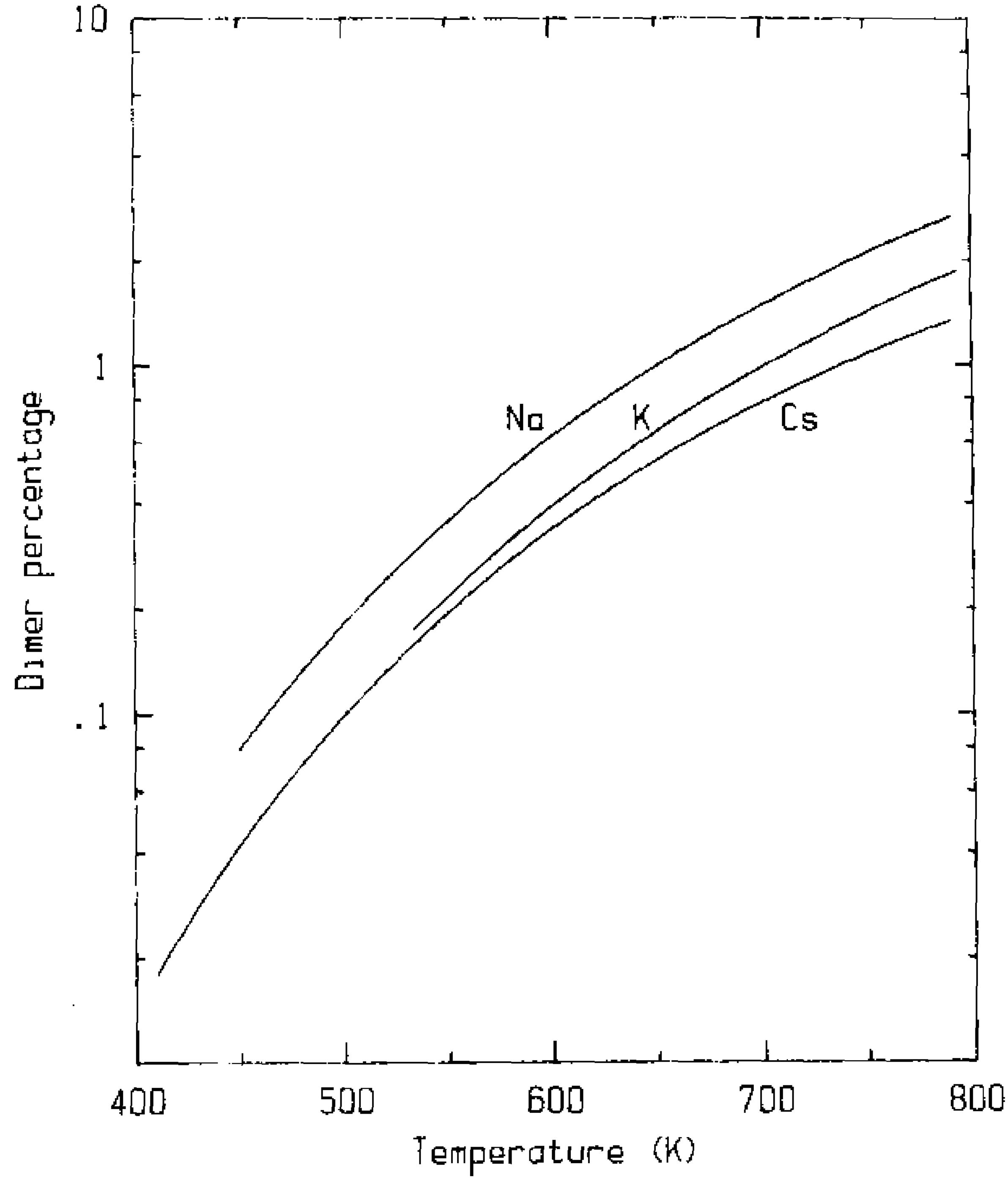

Fig.2.4. Dimer fraction in percentage for Na, K and Cs under chemical equilibrium.

the oven. It is believed that only a very thin surface layer of the metal piece is contaminated in the process from washing to insertion into in the vacuum chamber. Cesium is handled in a different way. It comes from the manufacturer in a sealed glass ampule. It will burn if the ampule is broken in air, and thus the ampule is broken and loaded into the oven while immersed in liquid nitrogen. The liquid nitrogen in the oven is then pumped out with the vacuum system. Thus, contamination is completely avoided.

2.3. Noise

There are two sources of extraneous signals in the experiments. First, as might be expected, some signals will be observed at the electron multipliers even with no target vapor in the collision region. This is primarily due to stray electrons which result from collisions of a fraction of the ion beam with electrostatic lenses and apertures. The signals of these "gas-out" electrons are small (about one-tenth of the authentic signals at high energy) and they are measured by turning the alkali beam away from the collision region and monitoring the background signals.

The second and more vexing source of extraneous signals is related to the presence of alkali atoms on the surfaces within the collision region. Even with no ion beam in the collision region, some negatively-charged particles are observed to desorb from the alkali-coated surface and arrive at the two particle multipliers. The intensity of these particles increases dramatically as one increases the partial pressure of oxygen or water vapor in the vacuum chamber and, in fact, can easily saturate both particle multipliers. This problem prevents one from using $H^- + O_2$ to calibrate the apparatus during the alkali experiments. These negatively-charged particles which come from alkali-coated surfaces include both electrons and anions; their production mechanisms are not known. Photoemission from the alkali-metal coated surfaces definitely constitutes one of the noise sources. This is evidenced by the fact that the extraneous signals increase dramatically when light is shined through a glass window into the vacuum chamber. In the absence of such a light source, photons originating in the arc-discharge ion source still produce problems. Another source of electron production could be chemical reactions on the surfaces. The excess energy released in the adsorption of an atom or molecule to the surface can be absorbed by an electron on the surface, allowing the electron to escape the Fermi sea. Chemical reactions on the surfaces may also result in the production of O^- and O_2^-. The energy defect for an adsorbed O or O_2 to capture a local electron and desorb from the surface is small since the "dirty" alkali-metal coated surface may have a much lower work function than a corresponding clean alkali-metal surface.

These extraneous signals caused by the alkali-coated surfaces increase, understandably, when the oven is heated up. The signals are found to decrease, however, when the temperature of the oven keeps increasing beyond a certain point, and fortunately, are about one-eighth of the authentic signals at the appropriate temperature to do the experiments. One of the reasons for this fortunate phenomenon could be that the regions from which negative particles produced on the surface can subsequently arrive at the particle multipliers are limited, and the change of the chemical composition in those regions, resulting from the increase in the alkali-metal vapor pressure, tends to reduce the production of negative particles.

The background signals from the alkali-metal surfaces are measured by steering the ion beam away from the collision region and observing the resultant signals present with a zero-intensity primary ion beam.

2.4. Data Acquisition

With the known methods to measure the extraneous signals, the authentic count rate N in the experiment is determined by subtraction

$$N = (N_1 - N_2) - (N_3 - N_4)$$

where N_1 is the count rate for beam-in and target-in, N_2 for beam-out (steer the beam away electrically) and target-in, N_3 for beam-in and target-out, and N_4 for beam-out and target-out. The relative cross sections are then obtained from

$$\sigma(E) = \frac{N(E)}{I(E)} f(E)$$

where I(E) is the intensity of the primary ion beam (the typical I(E) is in the order of 0.03 nA) and f(E) is the transmission function of the product collecting system, an example of which is given in Fig.2.2. The experimental data are acquired with an IBM Personal Computer (Model No. 5150), and the collision energy E is changed by changing the anode voltage with the computer. This semi-automatic control of the apparatus with the computer significantly reduces the time for each whole run, which is crucial for the alkali-metal experiments. It takes about 5 minutes to collect a complete set of curves for the cross sections for collision energies ranging from 3 to 300 eV. During a given run, the temperature change of the oven is limited to variations of approximately 0.2%. H^- and D^- beams are used alternatively and averaged for each projectile to minimize the error due to the temperature drift of the oven.

2.5. Error Analysis

Data obtained with the crossed-beam apparatus are reproducible to within 10%. With the transmission functions determined with H^- + O_2 (the reported cross sections, $\sigma_{ct}(E)$ and $\sigma_e(E)$, and their ratios, $\sigma_{ct}(E)/\sigma_e(E)$, are accurate to within 20% for this system[28]), earlier total cross section measurements for D^- + O_2 (accurate to within 20%, Ref. 28) and H^- + Ar (accurate to within 15%, Ref. 1) can be reproduced with the present apparatus to within the reported experimental uncertainties associated with those results. Combining these facts, we conclude that the systematic error associated with the present apparatus is less than 22% when the change in the target intensity is negligible.

The ratios, $\sigma_{ct}(E)/\sigma_e(E)$, do not depend upon the target intensity. Consequently errors in the measured ratios are limited to 22% (mainly attributed to calibration) for the alkali-metal targets.

The temperature drift of the oven during a complete cycle of the experiments is about 0.2%; the pressure change associated with this amount of temperature drift is about 4%. This error, combined with the systematic error of the apparatus, determines the accuracy for $\sigma(E_1)/\sigma(E_2)$ (either σ_{ct} or σ_e) to be 23%.

The ratios of cross sections, $\sigma^H(E)/\sigma^D(E)$, for different isotopes do not depend on the calibration.

Their errors are determined by the reproducibility of the apparatus and the stability of the target intensity; they are 11%.

Chapter 3

RESULTS AND DISCUSSION

3.1. Background of This Study

Due to their intrinsic theoretical interests and some practical concerns as discussed in section 1.2, slow collisions of H^- with alkali-metal atoms have recently been the focus of considerable attention. Theoretically, Karo et al.[32] performed multiconfiguration self-consistent-field (MCSCF) calculations for the potential curves of ground states of several alkali hydrides and their corresponding negative molecular ions. Olson and Liu[33] calculated configuration-interaction (CI) potential curves for the low-lying states of NaH and NaH^-, and based on their CI potential curves and a two-state perturbed-stationary-state (PSS) approximation, they estimated the charge transfer as well as the electron detachment cross sections for H^- + Na for energies below 400 eV. They also obtained the cross sections for H^- + K, Rb and Cs by scaling the results for H^- + Na to account for the different dipole polarizabilities and electron affinities of the alkali atoms. Experimentally, Meyer[34] measured total electron-loss cross sections for H^- + Cs in the energy range from 150 eV to 2 keV utilizing beam attenuation methods. Tuan and Esaulov[35] obtained differential energy-loss spectra of scattered H atoms for $H^- + Na$ with a time-of-flight apparatus and, based on the spectra, estimated the ratios of the charge transfer to the electron detachment cross sections for energies ranging from 100 to 500 eV.

For energies above about 500 eV, there have been a number of experiments in which the "equilibrium fractions" for collisions of hydrogen (and deuterium) atoms and ions with alkali vapors have been measured. A review of those measurements may be found in Schlachter et al.[36]

Nevertheless, the theoretical and experimental results reported so far have not been sufficient to elucidate the nature of the electron-loss mechanism for slow collisions of hydrogen negative ions with alkali atoms. First of all, theoretical discrepancies still appear to exist: Olson and Liu[33] state that there is no apparent crossing of the ionic $X^2\Sigma$ state into the $X^1\Sigma$ continuum, while the calculations by Karo et al.[32] indicate that such a crossing occurs in the region $R \approx 3a_0$. Olson and Liu[33] suggest that the principal mechanism for electron-loss is due to the long-range coupling between the $X^2\Sigma$ and $A^2\Sigma$ states of NaH^-; they predict the threshold energy for electron-loss to be around 15 eV with charge transfer dominating electron detachment for all energies below 400 eV. The potential calculations by Karo et al.[32], on the other hand, imply that detachment due to the coupling near the crossing between the $X^2\Sigma$ and $X^1\Sigma$ states is not negligible and has an energetic threshold close to zero. The experimental results tend to support the supposedly less accurate MCSCF potential curves: the differential energy-loss spectra of scattered H for H^- + Na measured by Tuan and Esaulov[35] show that the electron detachment is comparable in magnitude to the charge transfer, which leads them to conclude that detachment due to the coupling between the ionic $X^2\Sigma$ state and the $X^1\Sigma$ continuum is one of the main cause of the discrepancy between theory and experiment. Furthermore, the total electron-loss cross section of H^- + Cs measured by Meyer[34] is 2 to 3 times larger and, in addition, displays a much weaker energy dependence than that predicted by Olson and Liu. Finally, no direct cross section measurements of $\sigma_{ct}(E)$ or $\sigma_e(E)$ for collisions of H^- with alkali atoms have been reported in the low energy regime.

The purpose of the work described in this dissertation is to measure $\sigma_{ct}(E)$ and $\sigma_e(E)$ in slow collisions of H^- and D^- with Na, K and Cs.

3.2. $H^-(D^-)$ + Na

The measured cross sections for charge transfer, $\sigma_{ct}(E)$, and electron detachment, $\sigma_e(E)$, for collisions of

H^- with Na are shown in Fig.3.1 as functions of relative collision energy, and they are listed in Table 3.1. Since the target thickness in our crossed-beam experiments could not be measured accurately, the absolute value of the cross sections reported here were not experimentally determined. We have chosen to normalize $\sigma_{ct}(E)$ to Olson and Liu's calculation[33] at high energy in order to facilitate comparison. As may be seen in Fig.3.1, both charge transfer and electron detachment are significant electron-loss mechanisms in the H^- + Na collisions. $\sigma_{ct}(E)$ displays a strong energy dependence and a high energetic threshold (about 20 eV); the measured $\sigma_{ct}(E)$ agrees well with Olson and Liu's calculation. On the other hand, $\sigma_e(E)$ exhibits a weaker energy dependence and a near zero-energy threshold; the measured $\sigma_e(E)$ seriously disagrees with the prediction that $\sigma_e/\sigma_{ct} \leq 0.5$ (Ref.33). There are reasons for the agreement and the disagreement; they will become clear in the following discussion.

It is useful at this moment to refer to the potential curves for NaH and NaH^- in Fig.3.2. These potential curves represent eigenvalues of the Born-Oppenheimer Hamiltonian as functions of the internuclear separation R. These curves are obtained by means of a cubic-spline fit to the numerical results reported by Olson and Liu.[33] Their calculated asymptotic separation between the $X^2\Sigma$ and $X^1\Sigma$ states is 0.554 eV, deviating from the electron

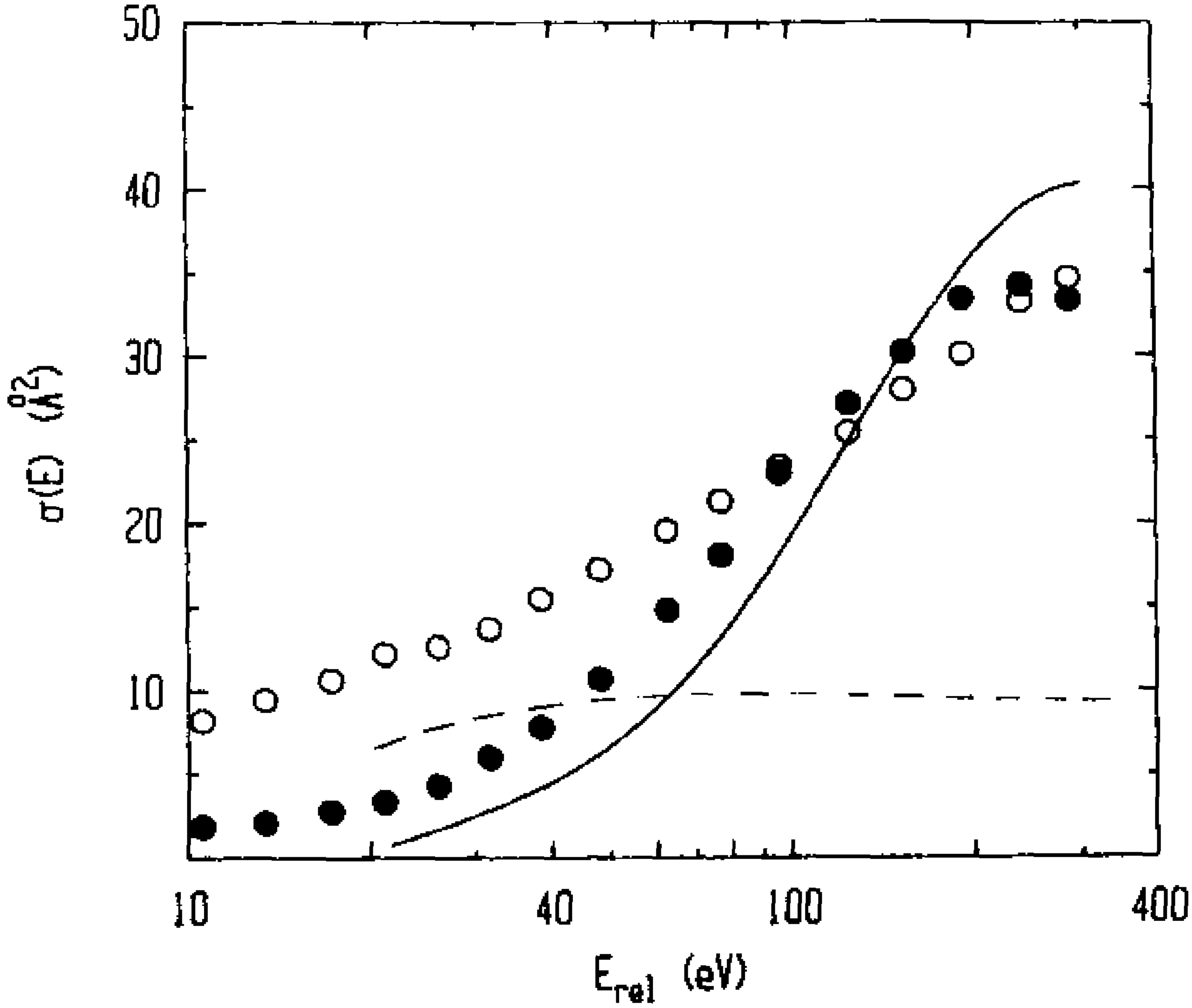

Fig.3.1. Measured $\sigma_{ct}(E)$ (solid circles) and $\sigma_e(E)$ (open circles). Solid line is the calculated $\sigma_{ct}(E)$ from Ref.33. Dashed line is the calculation of Eq.3.3 plus 6.4 $Å^2$ (see text).

TABLE 3.1

$\sigma_{ct}(E)$ and $\sigma_e(E)$ for H^- + Na

E_{rel} (eV)	σ_{ct} (Å^2)	σ_e (Å^2)
10.5	1.86	8.19
13.4	2.13	9.45
17.3	2.79	10.6
21.1	3.35	12.2
25.9	4.32	12.6
31.6	6.01	13.7
38.3	7.81	15.5
47.9	10.7	17.3
62.3	14.8	19.6
76.7	18.1	21.3
95.8	23.0	23.4
125	27.1	25.4
153	30.2	27.9
192	33.4	30.1
240	34.2	33.2
288	33.3	34.6

Note: σ_{ct} are normalized to Olson and Liu's calculation[33] at about E = 150 eV.

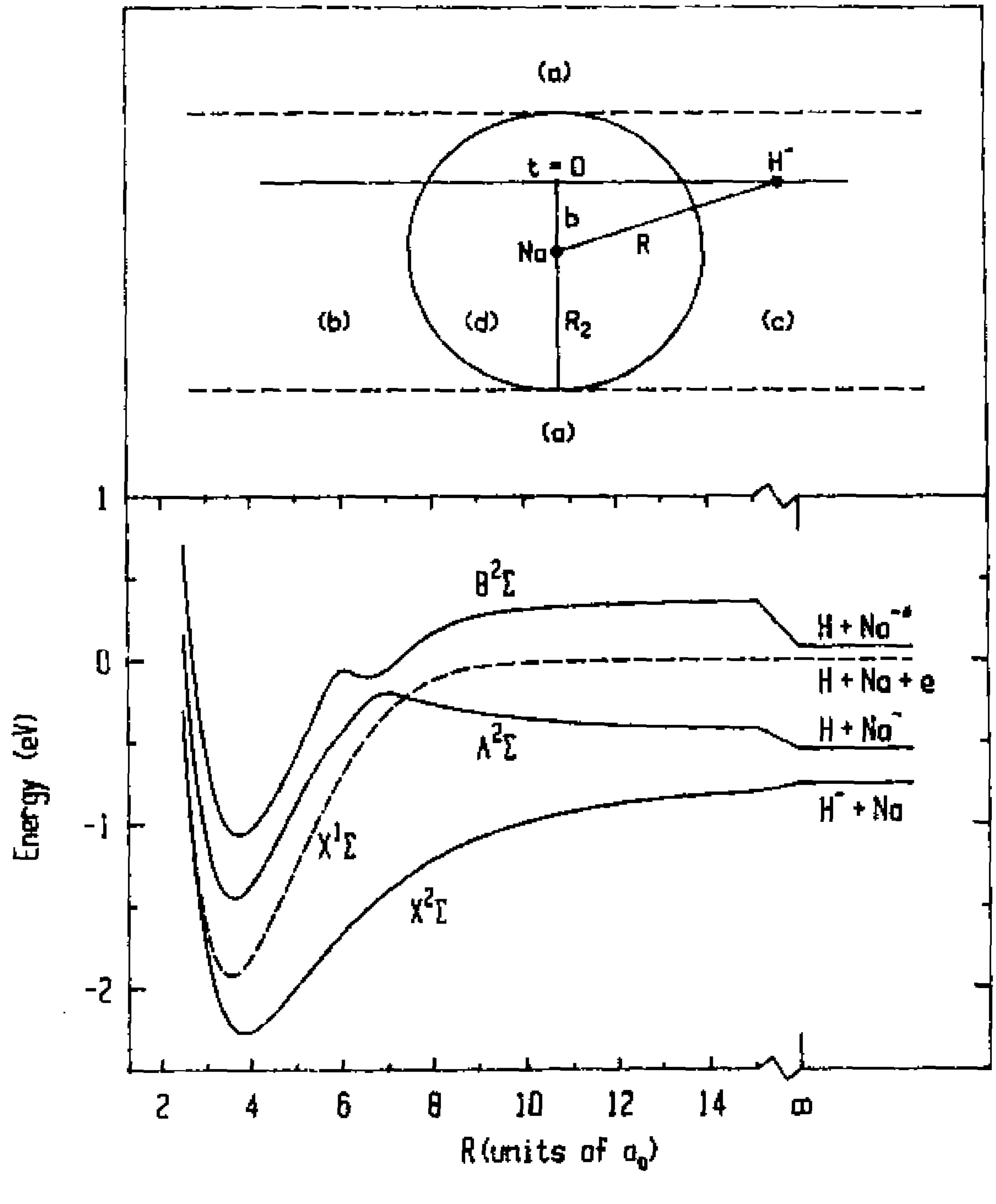

Fig.3.2. Low-lying molecular states of NaH^- (solid lines) and ground state of NaH; from Ref.32. The upper portion of the figure indicates the various regions (a-d) which are used to discuss the collision dynamics for this system.

affinity of hydrogen by 0.20 eV (presumably because the correlation energy between the core and valence electrons was not included for NaH^-, whereas it was for NaH). Therefore, the curves shown in Fig.3.2 for the negative ionic states have been shifted down relative to the neutral molecular state to compensate for this asymptotic error. As may be seen, even with such adjustment, the $X^2\Sigma$ state still crosses into the $X^1\Sigma$ continuum around $R = 2.7\ a_o$ (denoted R_1 hereafter), agreeing with the MCSCF calculation by Karo et al.[32]

The calculations which show that the ground potential curve of NaH^- crosses into the continuum of NaH is supported by the measurements of the elastic differential cross sections of H^- + Na which have been carried out previously in this laboratory.[37] In the absence of any inelastic channel, the elastic differential cross section is determined solely by the ground potential which can be accurately predicted. A comparison of such a calculated cross section with the experimental results may thus reveal the presence of an inelastic channel. Both theoretical and experimental elastic differential cross sections for H^- + Na determined in this laboratory are shown in the Fig.3.3 in reduced coordinates. The calculated cross section depends very little upon the collision energy when presented in reduced coordinates, as in Fig.3.3, and it predicts no sharp decrease for $E\theta > 140$ eV

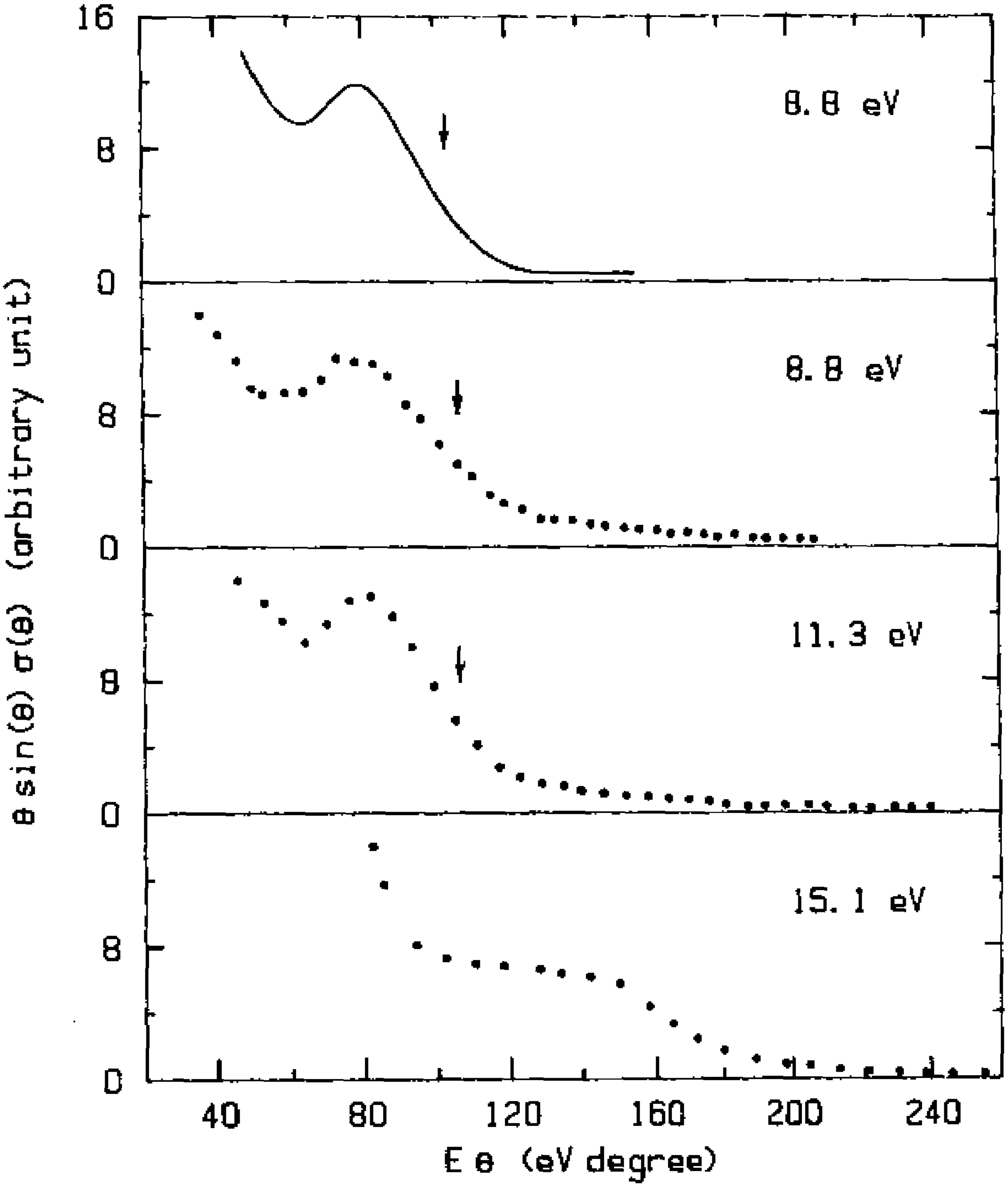

Fig.3.3. Reduced elastic differetial cross section [$\sigma(\theta)$ θ sin(θ)] versus reduced angle (Eθ) for H^{+} + Na. Line is Result of JWKB calculation. Dots are experimental measurements. The arrows mark the rainbow angles.

degree. On the other hand, a sharp depletion in the elastic differential cross sections in the 15.1 eV experiment is observed at the reduced angle $E\theta \approx 150$ eV degree. This angle corresponds to a trajectory with the classical turning point $R_{tp} \approx 2.7\ a_o$. The sharp depletion indicates the onset of an electron-loss channel of H^- and strongly suggests that the ground NaH^- state does in fact cross into the NaH continuum around $R = 2.7\ a_o$.

Let us neglect other electron-loss channels at the moment and consider only the direct detachment for $H^- + Na$ due to the crossing between $X^2\Sigma$ and $X^1\Sigma$. This system then resembles H^- + rare-gas systems, where the detachment cross section can be reasonably estimated with the simplest version of the curve crossing model.[2] In its simplest form, the model assumes that the detachment probability is a step function

$$P(b,E) = \begin{cases} 0 & \text{for} \quad b \geq b_x(E) \\ 1 & \text{for} \quad b < b_x(E) \end{cases}$$

where b_x is the impact parameter for which the classical turning point of the nuclear motion is exactly the crossing point between the ionic state and the neutral continuum. This version of the model thus predicts

$$\sigma_e(E) = \pi b_x^2 = \pi R_x^2 \left[1 - \frac{V(R_x)}{E}\right]$$

where R_x is the internuclear separation at the crossing, and V(R) is the molecular potential energy of the ionic state. For the $H^- + Na$ system, the ionic $X^2\Sigma$ state crosses into the neutral $X^1\Sigma$ continuum at $R = R_1$, and $V(R_1)$ is approximately zero. Thus, the direct detachment may yield a cross section as high as $\pi R_1{}^2$ or 6.4 $Å^2$ and its threshold energy will be near zero.

Now that we have an estimate of the direct detachment of H^- due to the crossing between the $X^2\Sigma$ state and the $X^1\Sigma$ continuum, let us consider the electron loss of H^- via the charge exchange between the $X^2\Sigma$ and $A^2\Sigma$ states. These two states are the ground and the first excited states of the quasi-molecular ion NaH^- and correspond asymptotically to $H^- + Na$ and $H + Na^-$, respectively, in the separated atom limit. Since they are eigenstates of the electronic Hamiltonian, there is no overlap between their electronic wavefunctions $\phi_1^a(r,R)$ and $\phi_2^a(r,R)$ or $<\phi_1^a|\phi_2^a> = 0$.

For an extremely slow collision, the electrons behave adiabatically, staying always in a continuously adjusting eigenstate of the electronic Hamiltonian. If the initial state is $H^- + Na$, the electronic wave function for the process can be written as

$$\Phi_1(r,t) = T_1(t)\ \phi_1^a[r,R(t)]$$

The time-dependent factor $T_1(t)$ is determined from the Schrödinger equation to be

$$T_1(t) = \exp[\frac{1}{i\hbar}\int_{-\infty}^{t} h_{11}^{a}(R)\ dt],$$

Thus

$$\Phi_1 = \phi_1^a(r,R)\ \exp[\frac{1}{i\hbar}\int_{-\infty}^{t} h_{11}^{a}(R)\ dt]$$

Accordingly, the electronic wave function is

$$\Phi_2 = \phi_2^a(r,R)\ \exp[\frac{1}{i\hbar}\int_{-\infty}^{t} h_{22}^{a}(R)\ dt]$$

if the initial state is H + Na^+.

As the collision velocity increases, the electrons can only imperfectly adjust to the changing molecular field, and transitions occur. Generally, we may consider the electronic wavefunction as lagging behind in the collision by an infinitesimal time interval dt, or at time t the wave function is $\Phi_1(r,t-dt)$. This wavefunction now overlaps with $\Phi_2(r,t)$ to a certain degree and this can lead to transitions. The transition amplitude

$$dB_2^a = \langle\Phi_2(r,t)\,|\,\Phi_1(r,t-dt)\rangle$$

$$= \frac{1}{i\hbar}\ \langle\phi_2^a|\ v\cdot P\ |\phi_1^a\rangle\ \exp[\frac{1}{i\hbar}\int_{-\infty}^{t}(h_{22}^{a} - h_{11}^{a})\ dt]\ dt$$

Once the system is in the charge exchanged $A^2\Sigma$ state, it may make further transitions to other states. The possible transitions from $A^2\Sigma$ will be discussed in the following paragraph.

The molecular potential curves shown in Fig.3.2 exhibit an avoided crossing between the $A^2\Sigma$ and $B^2\Sigma$ states around $R = 6.8\ a_o$ (denoted R_2 hereafter). The $A^2\Sigma$ state thus suddenly changes its "character" at the avoided crossing. For $R > R_2$, the $A^2\Sigma$ state has an approximate $H + Na^-$ electronic configuration and its active electronic wavefunction has 3s-wave character; the system in the $A^2\Sigma$ state is expected to decay quickly when $A^2\Sigma$ crosses into the $X^1\Sigma$ continuum around $R = 7.4\ a_o$ (denoted R_3 hereafter). For $R < R_2$, the $A^2\Sigma$ state lies entirely within the $X^1\Sigma$ continuum; and it may illusively appear that the $X^2\Sigma$ - $A^2\Sigma$ coupling in this region is not important because the coupling between a localized wave and a free-electron wave is small. However for $R < R_2$ the $A^2\Sigma$ state becomes a shape resonance because of its large p atomic wave component. The neutral quasi-molecule NaH is mainly in the ionic Na^+H^- configuration for small R. Its negative ion can be understood by assuming that an active electron moves in the field of the neutral molecular "core", Na^+H^-, which remains essentially unchanged over a large range of internuclear separation. The active electron tends to stay closer to Na^+, and its ground state, $X^1\Sigma$, has an approximate 3s atomic wave character, while its first exited state, $A^2\Sigma$, is a 3p wave-like state. It follows that the $A^2\Sigma$ state is a shape resonance[38] and cannot decay easily because of the p-wave centrifugal barrier. A shape resonance has a localized wave and thus the $X^2\Sigma$ - $A^2\Sigma$ coupling for $R < R_2$ could be significant. The outcome of this coupling depends on the lifetime (which is not known yet) of the $A^2\Sigma$ shape resonance. If the lifetime is shorter than the collision time, which is on the order of 10^{-15} second, the $A^2\Sigma$ state will decay directly into the $X^1\Sigma$ state by emitting an electron; otherwise, it may transit to the $B^2\Sigma$ state around the avoided crossing and end up in the final products of H + Na^{-*} (Ref.39,40). Na^{-*} then autodetaches. For any of these scenarios, the $X^2\Sigma$ - $A^2\Sigma$ coupling for $R < R_2$ will contribute to electron detachment channel.

To summarize, the transitions from the $A^2\Sigma$ state to other states mainly happen within a sphere of $R < R_3$ defined in the internuclear separation space. Various effects associated with the $X^2\Sigma$ - $A^2\Sigma$ coupling can thus be identified by dividing the internuclear separation space into regions as follows:

$$X^2\Sigma - A^2\Sigma \begin{cases} R > R_3 \begin{cases} b > R_3 & \text{-------------------- (a)} \\ b < R_3 \begin{cases} t > 0 & \text{----------- (b)} \\ t < 0 & \text{----------- (c)} \end{cases} \end{cases} \\ R < R_2 & \text{----------------------------- (d)} \end{cases}$$

where $t < 0$ corresponds to the incoming trajectory (taken to be a straight line). These regions are illustrated in the upper portion of Fig.3.2. The coupling in regions (a) and (b) can only lead to charge transfer. In (c), on the other hand, charge exchange to the $A^2\Sigma$ state will result in a subsequent crossing into the $X^1\Sigma$ continuum at $R = R_3$, leading to electron detachment. In (d), the $A^2\Sigma$ state will decay into the $X^1\Sigma$ continuum either directly or via a shape resonance Na^{-*}.

It is clear that the cross sections for charge transfer and electron detachment due to the $X^2\Sigma$ - $A^2\Sigma$ coupling can be calculated without difficulty if information about the $\langle\phi_2^a|v\cdot P|\phi_1^a\rangle$ coupling term is available. Unfortunately, this term is not yet known and is apparently more difficult to calculate than the Hamiltonian matrix. One way out of this difficulty is to assume a form for the coupling term which contains some adjustable parameters, e.g., $\beta \exp(-\gamma R)$, and attempt to fit the experimental results. This method yields a semi-empirical interpretation. Another approach is to guess the diabatic potential curves; the diabatic coupling term can then be determined from

$$h_{12}^d = \frac{1}{2}\left[(h_{22}^a - h_{11}^a)^2 - (h_{22}^d - h_{11}^d)^2\right]^{1/2} \qquad (3.1)$$

In the two-state PSS calculation presented by Olson and Liu,[33] point-charge-induced dipole interaction potentials $(\alpha/2R^4)$ are assumed for the diabatic curves, $h_{11}^d(R)$ and $h_{22}^d(R)$, at large R. By fitting in the range $R = 10\text{-}20\ a_o$, they obtained an exponential form for h_{12}^d,

$$h^d_{12}(R) = \beta \exp(-\gamma R)$$

where $\beta = 0.7456$ eV and $\gamma = 0.171\ a_o^{-1}$.

To understand the above assumption for the diabatic curves, let us decompose the adiabatic potentials. The adiabatic potentials are composed of: (1) the dipole interaction between the negative ion and the polarized atom; (2) the charge exchange interaction between the electronic $H^- + Na$ and $H + Na^-$ configurations. The charge exchange interaction means that the molecular $X^2\Sigma$ state is allowed to have some component of the $H + Na^-$ configuration and this "extra" freedom to adjust lowers the energy of the $X^2\Sigma$ state. The same interaction raises the energy of the $A^2\Sigma$ state. This configuration mixing is considered to be responsible for the significance of $<\phi^a_2|v\cdot P|\phi^a_1>$. Since the assumed diabatic potentials do not include the charge exchange interaction, the coupling $<\phi^d_2|v\cdot P|\phi^d_1>$ is small.

With the known diabatic Hamiltonian matrix $\underline{h}^d$, the adiabatic coupling $(v\cdot\underline{P})^a_{12}$ is found from equation (1.4) to be

$$(v\cdot\underline{P})^a_{12} = -i\hbar v_R[(\frac{4}{R} - \gamma)\frac{\alpha}{R^4} - \Delta(\infty)\gamma]\frac{h^d_{12}(R)}{\Delta(R)^2}$$

where $\Delta(R)$ is the energy gap between the adiabatic potentials whose analytical form is given by equation

(3.1). The adiabatic coupling $(v\cdot\underline{P})^{a}_{12}$ on the b = 0 trajectory is shown in Fig.3.4 for collision energies E = 50 and 300 eV; also shown in the figure is the diabatic coupling $h^{d}_{12}(R)$ to serve as a comparison. The energy gaps between two potential curves for both representations are compared in Fig.3.5.

The amplitude $B^{a}_{2}(t)$ on the $A^{2}\Sigma$ state can then be calculated from perturbation methods if one assumes that the transition amplitude is small. Assuming that the nuclei move along straight-line trajectories, we have

$$B^{a}_{2}(b,v,x) = \frac{1}{i\hbar v}\int_{-\infty}^{x}(v\cdot\underline{P})^{a}_{12}\ \exp(i\theta)\ dx'$$

with

$$\theta(b,v,x) = \frac{1}{\hbar v}\int_{-\infty}^{x}(h^{a}_{22} - h^{a}_{11})\ dx'$$

where x is vt (t = 0 at the turning point, see Fig.4.2). Since the assumed diabatic potentials are good only for $R > R_3$ and the coupling mechanisms within $R < R_3$ are not precisely known, the above formulas for $B^{a}_{2}(b,v,x)$ are valid only in regions (a) and (c).

The resultant charge transfer cross section in the region (a) is

$$\sigma_{ct}(v) = \int_{R_3}^{\infty}|B^{a}_{2}(b,v,\infty)|^{2}\ 2\pi b\ db \qquad (3.2)$$

The corresponding electron detachment cross section

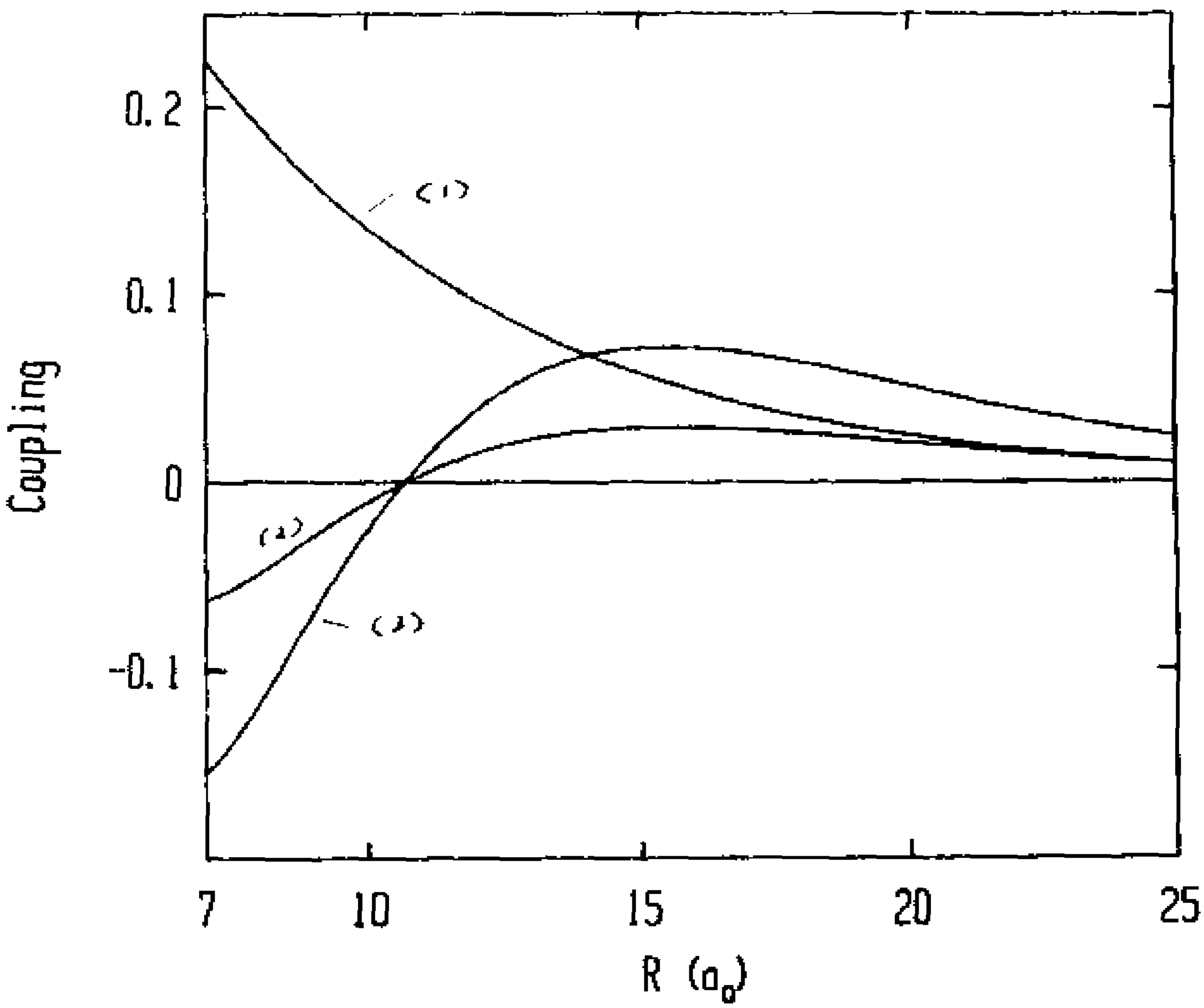

Fig. 3.4. Curve (1) is diabatic coupling $h^d_{12}(R)$. Curves (2) and (3) are adiabatic coupling $(\mathbf{v}\cdot\underline{P})^a_{12}$ on the b-0 trajectory for collision energies of 50 and 300 eV, respectively.

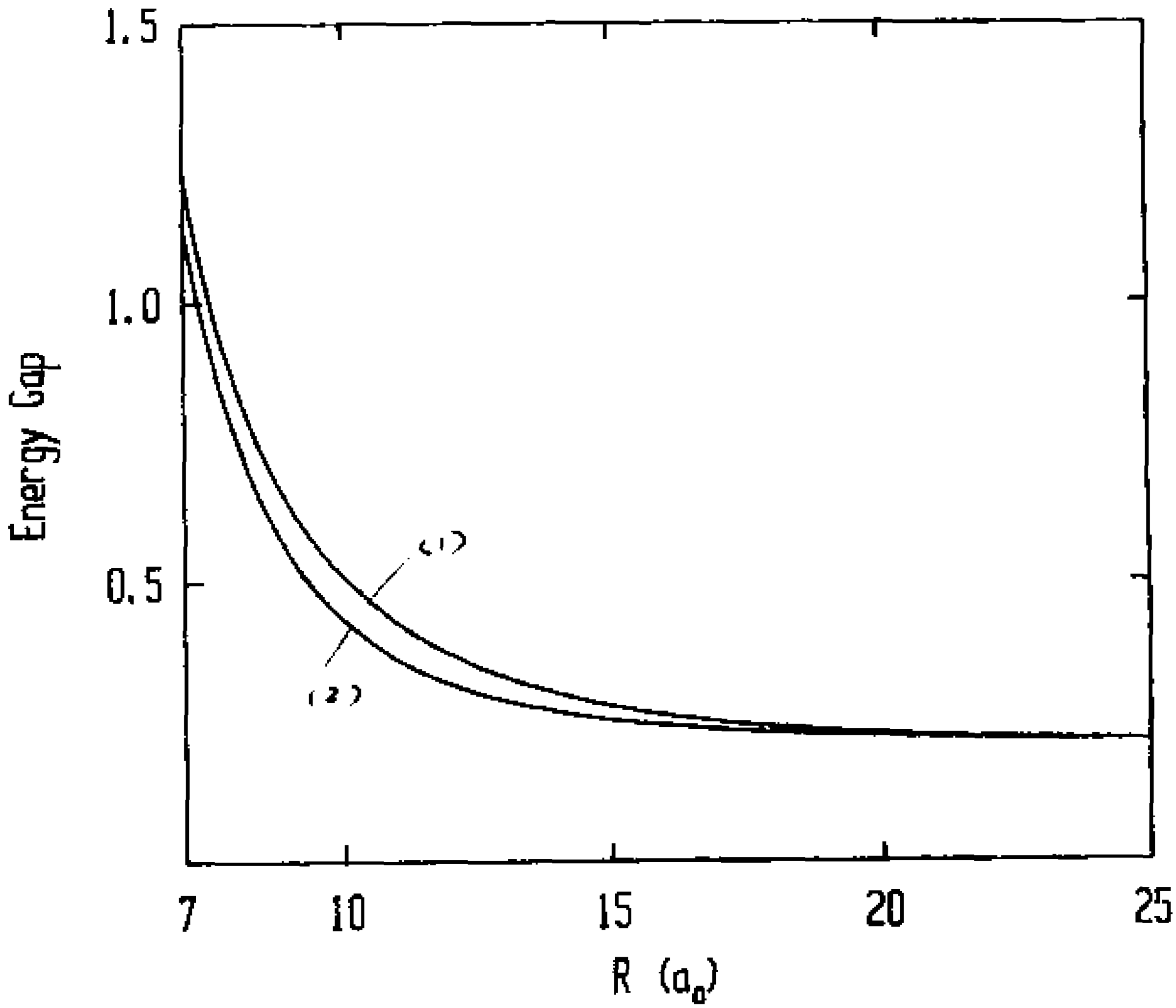

Fig.3.5. Curve (1) is the adiabatic energy gap and (2) is the diabatic energy gap.

in the region (c) is

$$\sigma_e(v) = \int_o^{R_3} |B_2^a[b,v,-(R_3^2 - b^2)^{1/2}]|^2 \; 2\pi b \; db \; . \qquad (3.3)$$

Numerical calculations of cross sections, based on these description, have been performed. The evolution of the probabilities in the charge exchanged $A^2\Sigma$ state along a trajectory with $b = 10\ a_o$ are shown in Fig.3.6 for collision energies 50 and 300 eV, and those along the $b = 0$ trajectory are shown in Fig.3.7. The final probabilities $|B_2^a|^2$ in the (a) region are shown in Fig.3.8 as functions of impact parameter b for $E = 50$ eV and $E = 300$ eV; those in the (c) region are shown in Fig.3.9. It may be seen that the final probability in (a) is much more energy dependent than that in (c). This is because the high collision velocity allows the transition to occur at a larger internuclear separation, and the "effective volume" for the transition in (a) increases faster with increase of collision velocity than that in (c). The final probabilities $|B_2^a|^2$ for $b = 0$ and $10\ a_o$ are shown in Fig.3.10 as functions of collision energy.

The cross sections calculated for the $X^2\Sigma$ - $A^2\Sigma$ coupling in regions (a) and (c) are listed in Table 3.2. Since the calculated molecular potentials for NaH include the correlation energy between the valence electrons and the inner molecular core while those for NaH^- do not, and they have been relatively shifted in the molecular

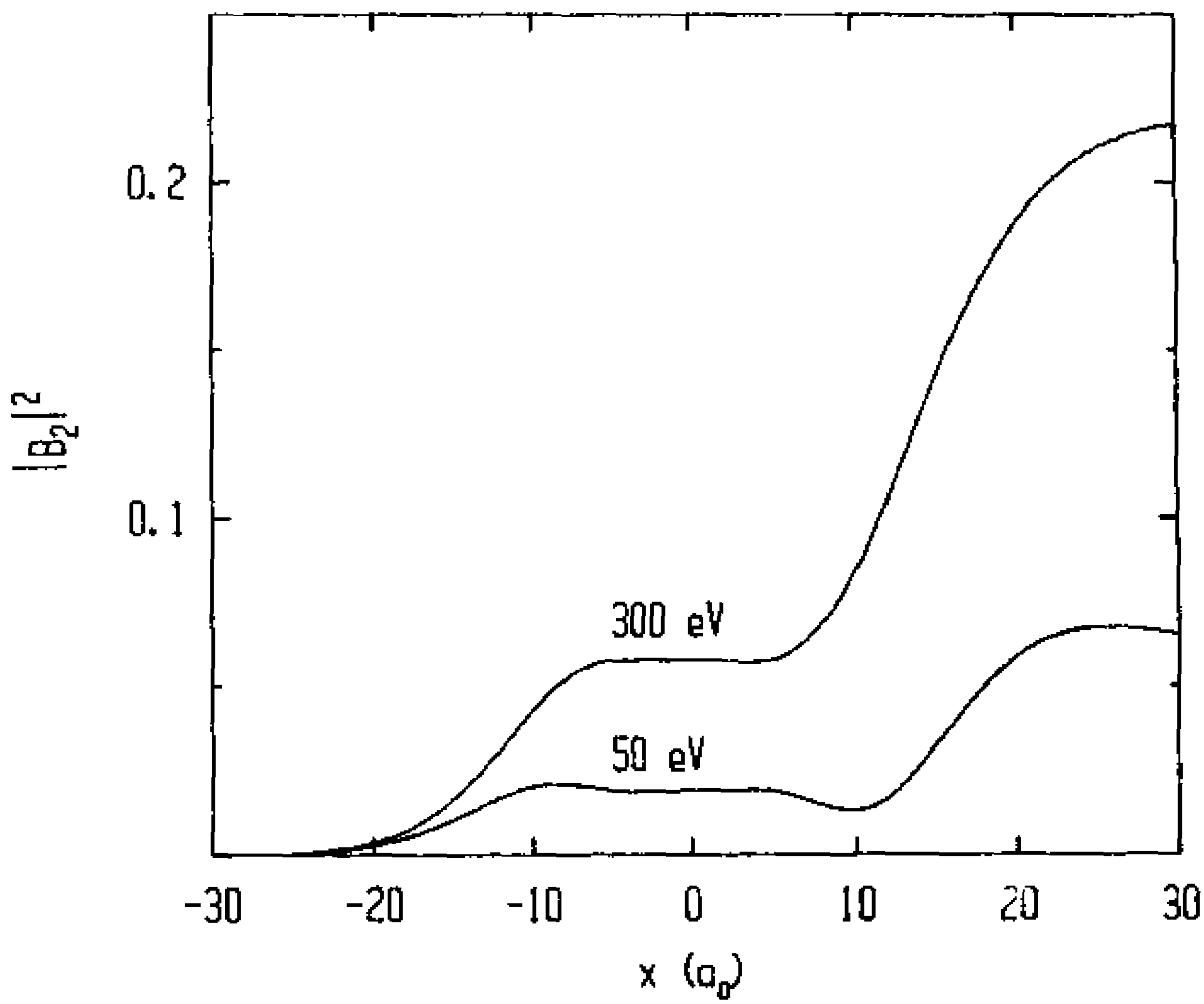

Fig.3.6. Evolution of probabilities in the $A^2\Sigma$ state along a trajectory with b = 10 a_o.

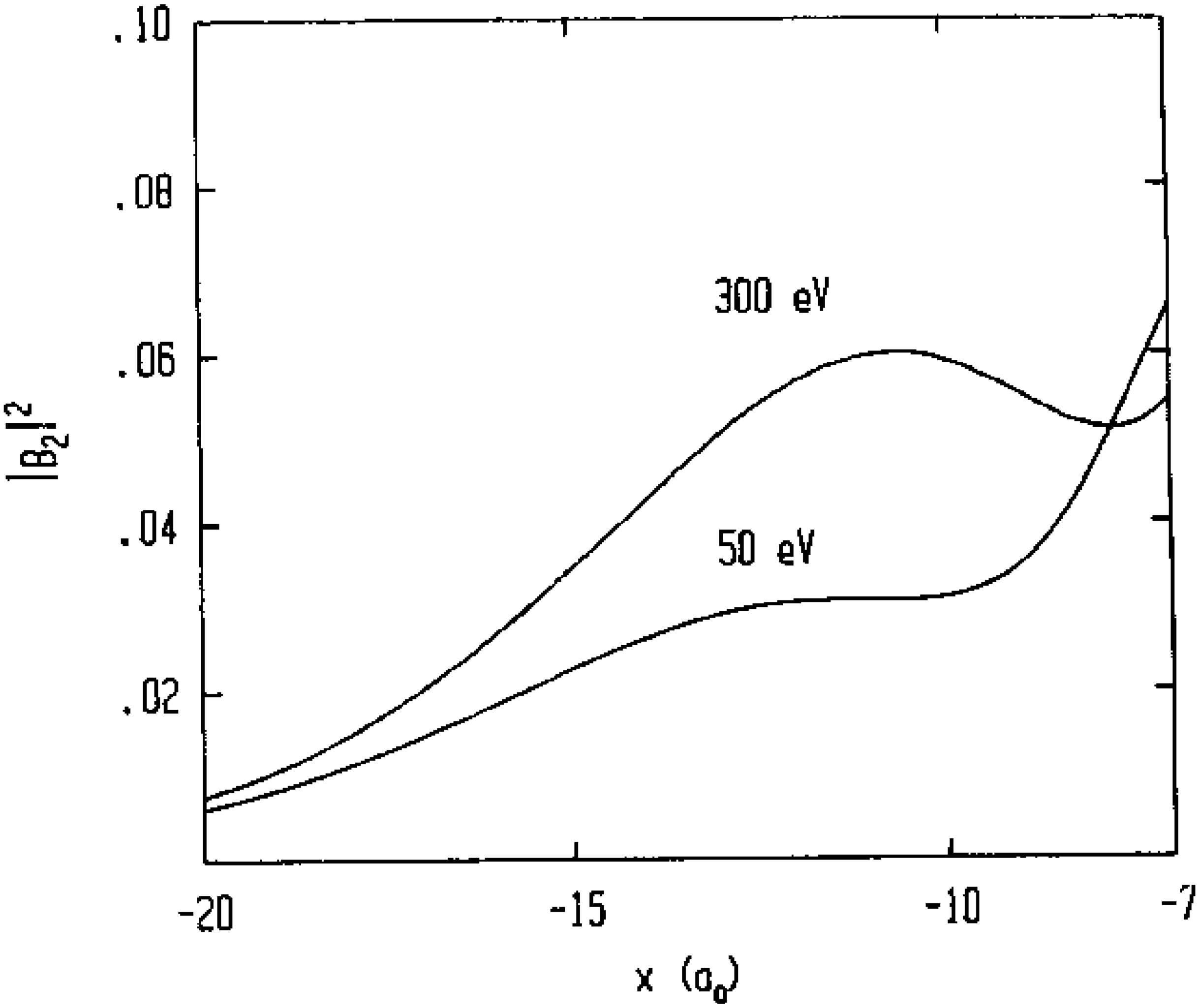

Fig.3.7. Evolution of probabilities in the $A^2\Sigma$ state along the b = 0 trajectory.

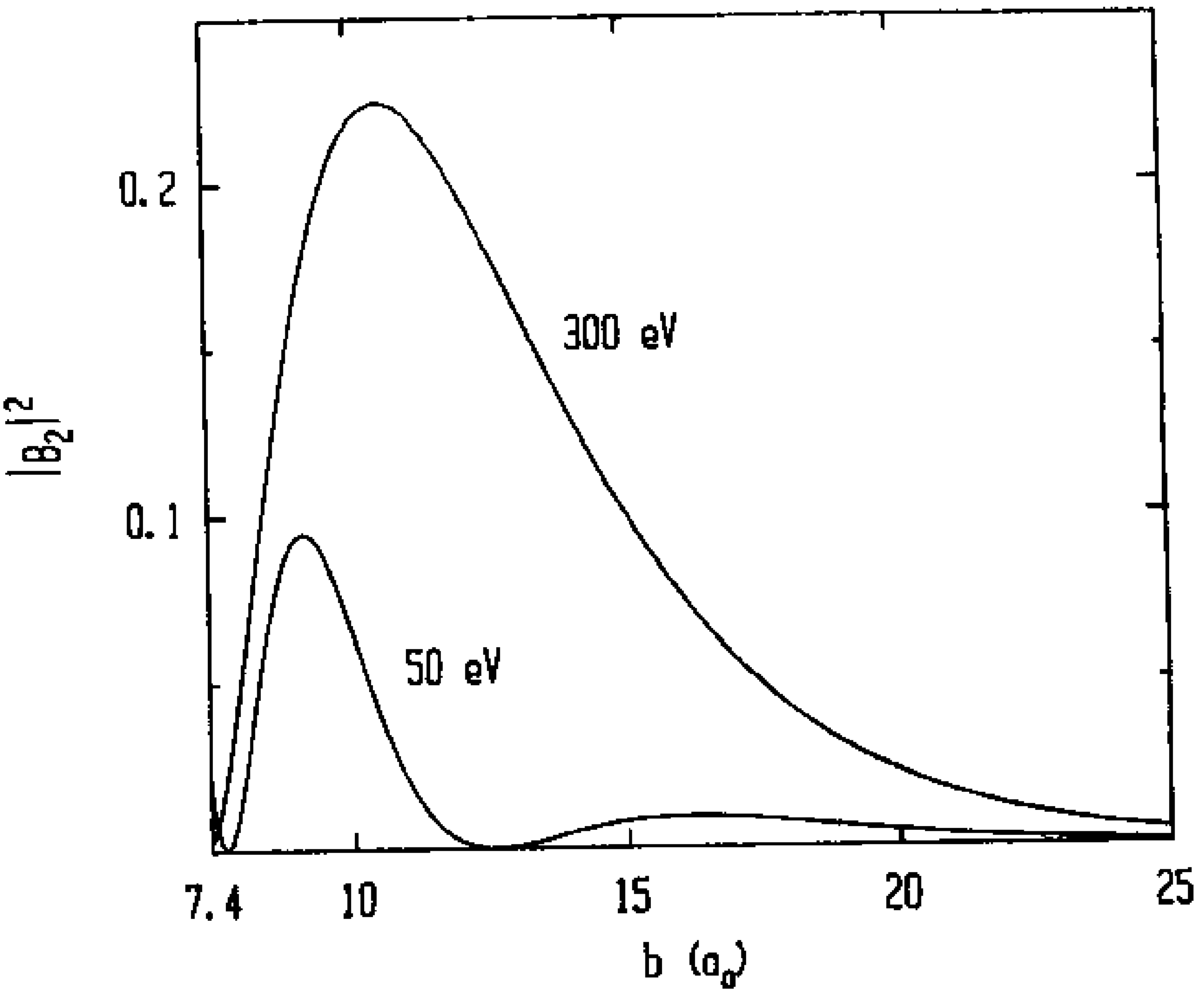

Fig.3.8. Final probabilities in the $A^2\Sigma$ state in region (a) as functions of b.

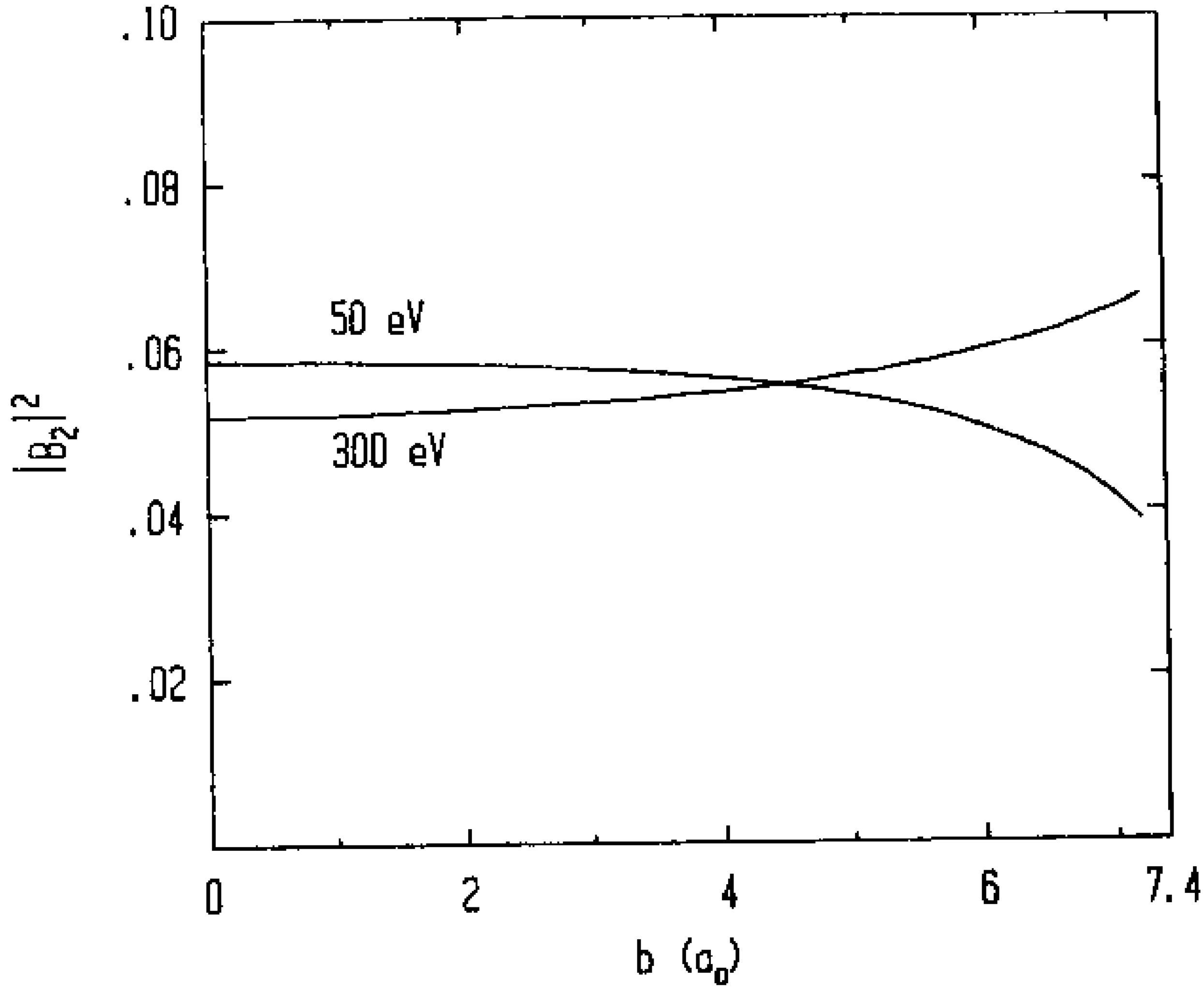

Fig.3.9. Final probabilities in the $A^2\Sigma$ state in region (c) as functions of b.

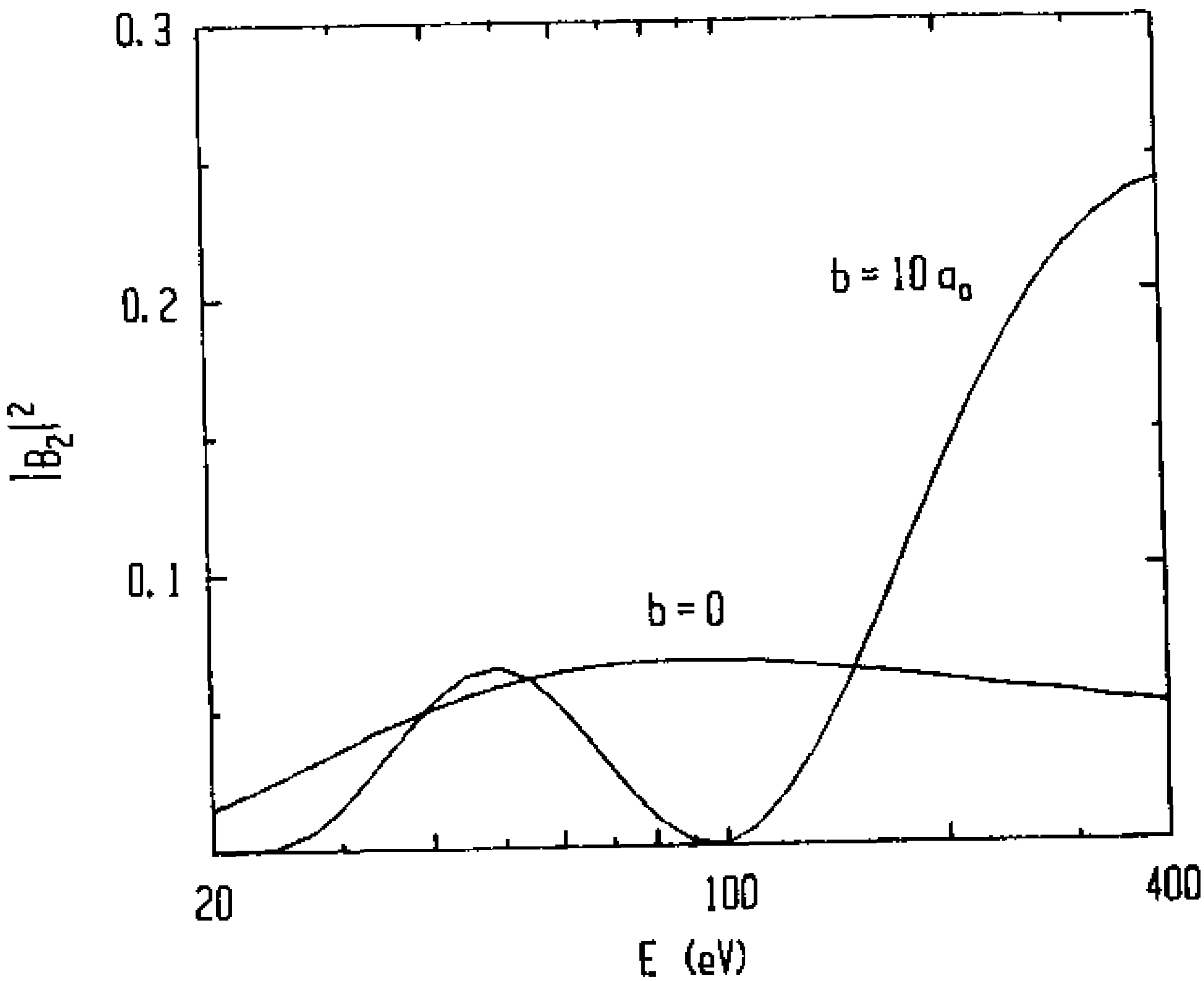

Fig.3.10. Final probabilities versus collision energy: $|B_2^a|^2$ at $x = -R_3$ for $b = 0$; $|B_2^a|^2$ at $x = \infty$ for $b = 10$.

TABLE 3.2

PSS Calculations for the $X^2\Sigma$-$A^2\Sigma$ Coupling

in region (a)

E_{rel} (eV)	$R_3 = 7.4\ a_o$	$R_3 = 8\ a_o$	Ref.33*
20	0.310	0.296	0.94
50	5.18	5.13	6.8
100	17.9	15.9	19
200	29.9	29.7	37
300	33.9	33.7	40

in region (c)

E_{rel} (eV)	$R_3 = 7.4\ a_o$	$R_3 = 8\ a_o$	Ref.33
20	0.354	0.472	0.36
50	2.49	2.45	2.1
100	3.34	3.24	5.3
200	3.12	3.26	6.0
300	2.83	3.14	4.5

* These results are believed to be the sum of the integrals in region (a) and (b) with the integral in (b) being taken to be equal to the integral in (c).

potential schematic shown in Fig.3.2 to compensate the asymptotic error, there is uncertainty about where the $A^2\Sigma$ state crosses into the $X^1\Sigma$ continuum. For this reason, we have calculated the cross sections for $R_3 = 7.4$ and $8\ a_o$.

There is discrepancy between the result of this work for the $X^2\Sigma$ - $A^2\Sigma$ coupling in the (c) region and the corresponding results calculated by Olson and Liu.[33] One of reasons for this discrepancy could be that we assume that $B_1^a(t) = 1$ for this calculation while they did not. Another reason could be that they used different parameters (which have not been reported).

The contribution to charge transfer from the (b) region is not included in this calculation, due to a lack of information about the coupling in the (d) region. However this contribution has an upper limit given by the integral (3.3). Olson and Liu's results for this integral, plus the calculated (this work) charge transfer from the (a) region, is in excellent agreement with Olson and Liu's total charge transfer cross sections. This implies that the only disagreement between their calculation and the one presented here can be attributed to the (c) region.

Let us now consider the additional electron detachment channels. In the above two-state PSS calculation, only one out of three channels which can lead to electron detachment are taken into account. The other two channels are: the $X^2\Sigma$ -$A^2\Sigma$ coupling in the (d) region ($R < R_2$) and the crossing of the $X^2\Sigma$ state into the $X^1\Sigma$ continuum at $R = R_1$. Since the survival probabilities of H^- are large, we can, to first order, treat the various electron-loss channels independently. Clearly, the $X^2\Sigma$ - $X^1\Sigma$ crossing contributes a maximum of $\pi R_1{}^2$ to electron detachment. This, combined with the calculated electron detachment due to the $X^2\Sigma$ - $A^2\Sigma$ coupling in the (c) region, is shown by the dashed line in Fig.3.1. The gap between the dashed line and the measured electron detachment cross sections shows an energy dependence similar to the charge transfer cross sections. This strong energy dependence suggests that there exists another electron loss channel that is near resonant in nature,[22] and this channel is thought to be the $X^2\Sigma$ - $A^2\Sigma$ coupling in the (d) region.

The detachment due to $X^2\Sigma$ - $A^2\Sigma$ coupling in the (d) region could not be estimated independently since the coupling term in the region is not known yet; its role in electron detachment which is suggested by our measurements has also been discussed previously by Tuan and Esaulov.[35] Tuan and Esaulov measured differential energy-loss spectra of scattered H atoms in collisions of H^- + Na with a time-of-flight apparatus. The spectra for a collision energy of 500 eV suggest that the Na^{-*} shape resonance[39,40] plays a role comparable to that for charge transfer to Na^-. It is clear from the molecular potentials that the $X^2\Sigma$ - $A^2\Sigma$

coupling in the (d) region is the most probable channel to lead to the shape resonance Na^{-*}. Secondly, the $A^2\Sigma$ state in the (d) region is mainly the H^- + Na(3p) electronic configuration. The larger collisional transition from H^- + Na(3S) to H^- + Na(3P) can be attributed to the large polarizability of Na. When H^- approaches Na, the electron wave around Na gets deformed, i.e., a p-wave component appears.

The importance or role of the short-range $X^2\Sigma$ - $A^2\Sigma$ coupling in such collisions could be investigated by studying photon production in "cleaner" systems such as Cl^- + Na. For the Cl^- + Na system, both molecular Cl^- + Na(3s) and Cl^- + Na(3p) states lie below the Cl + Na continuum and the Cl + Na^{-*} shape resonance; they thus form an ideal two-state system. The coupling between these two states will be short range in nature because of the large exothermicity.

In summary, for charge transfer in slow collisions of H^- with Na, the mechanism is simply the long-range coupling between $X^2\Sigma$ and $A^2\Sigma$; a previous calculation[33] agrees well with our measurements. For the electron detachment, on the other hand, there are several responsible mechanisms: (1) autodetachment due to the crossing of $X^2\Sigma$ into $X^1\Sigma$; (2) charge transfer to $A^2\Sigma$ for $b < R_3$ and $t < 0$ and thereafter detachment due to the crossing of $A^2\Sigma$ into $X^1\Sigma$; (3) charge transfer to the $A^2\Sigma$ resonance in

$R < R_2$ and thereafter detaching to $X^1\Sigma$ or transiting to $B^2\Sigma$ or $H + Na^{-*}$ shape resonance state due to the avoided crossing between $A^2\Sigma$ and $B^2\Sigma$.

The measurements of σ_{ct} and σ_e for collisions of D^- with Na (and H^- + Na) are shown in Fig.3.11 as functions of E/M, and they are listed in Table 3.3. As may be seen, both σ_{ct} and σ_e display velocity-dependent isotope effects which are consistent with the theories discussed above; the two-state PSS method with straight-line trajectories inherently contains a velocity-dependent isotope effect for H^- and D^-.

The experimental ratios, σ_{ct} / σ_e, for $H^-(D^-)$ + Na are presented in Fig.3.12. Also shown in Fig.3.12 are the ratios for H^- + Na estimated by Tuan and Esaulov[38] based on their measurements of the differential energy-loss spectra of the scattered H atoms. Their results are in good agreement with the present measurements at the higher collision energies.

3.3. $H^-(D^-)$ + K

The measurements of σ_{ct} and σ_e for collisions of H^- and D^- with K are shown in Fig.3.13 as functions of E/M, and they are listed in Tables 3.4 and 3.5. The experimental ratios, σ_{ct} / σ_e, for H^- + K are shown in Fig.3.14. As for Na, we have chosen to normalize the measured σ_{ct} for H^- + K to Olson and Liu's calculation[33] at high

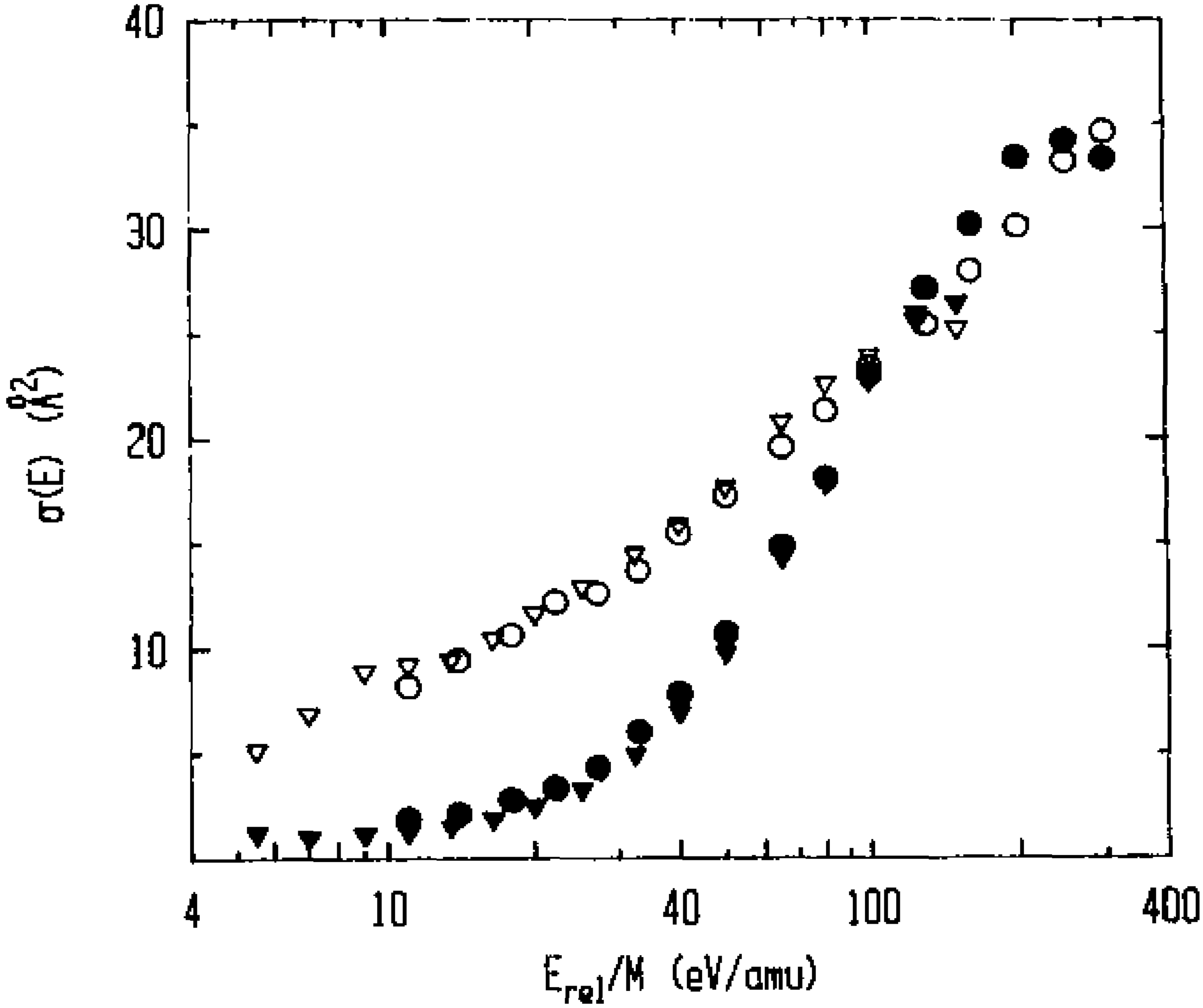

Fig.3.11. Measured σ_{ct} (solid symbols) and σ_e (open symbols) for H^- + Na (circles) and D^- + Na (triangles) versus E_{rel}/M, where E_{rel} is the relative collision energy and M the reduced mass of the projectiles.

TABLE 3.3

$\sigma_{ct}(E)$ and $\sigma_e(E)$ for D^- + Na

E_{rel} (eV)	σ_{ct} ($Å^2$)	σ_e ($Å^2$)
10.1	1.21	5.17
12.9	1.03	6.90
16.6	1.16	8.92
20.2	1.28	9.19
24.8	1.54	9.45
30.4	1.91	10.5
36.8	2.49	11.7
46.0	3.30	12.9
59.8	49.6	14.5
73.6	69.3	15.9
92.0	97.9	17.7
120	14.3	20.8
147	17.8	22.6
184	22.7	23.9
230	25.9	25.6
276	26.4	25.2

Note: the absolute values of σ_{ct} and σ_e for D^- are obtained by normalizing σ_{ct} for H^- to Olson and Liu's calculation[33] at about E = 150 eV.

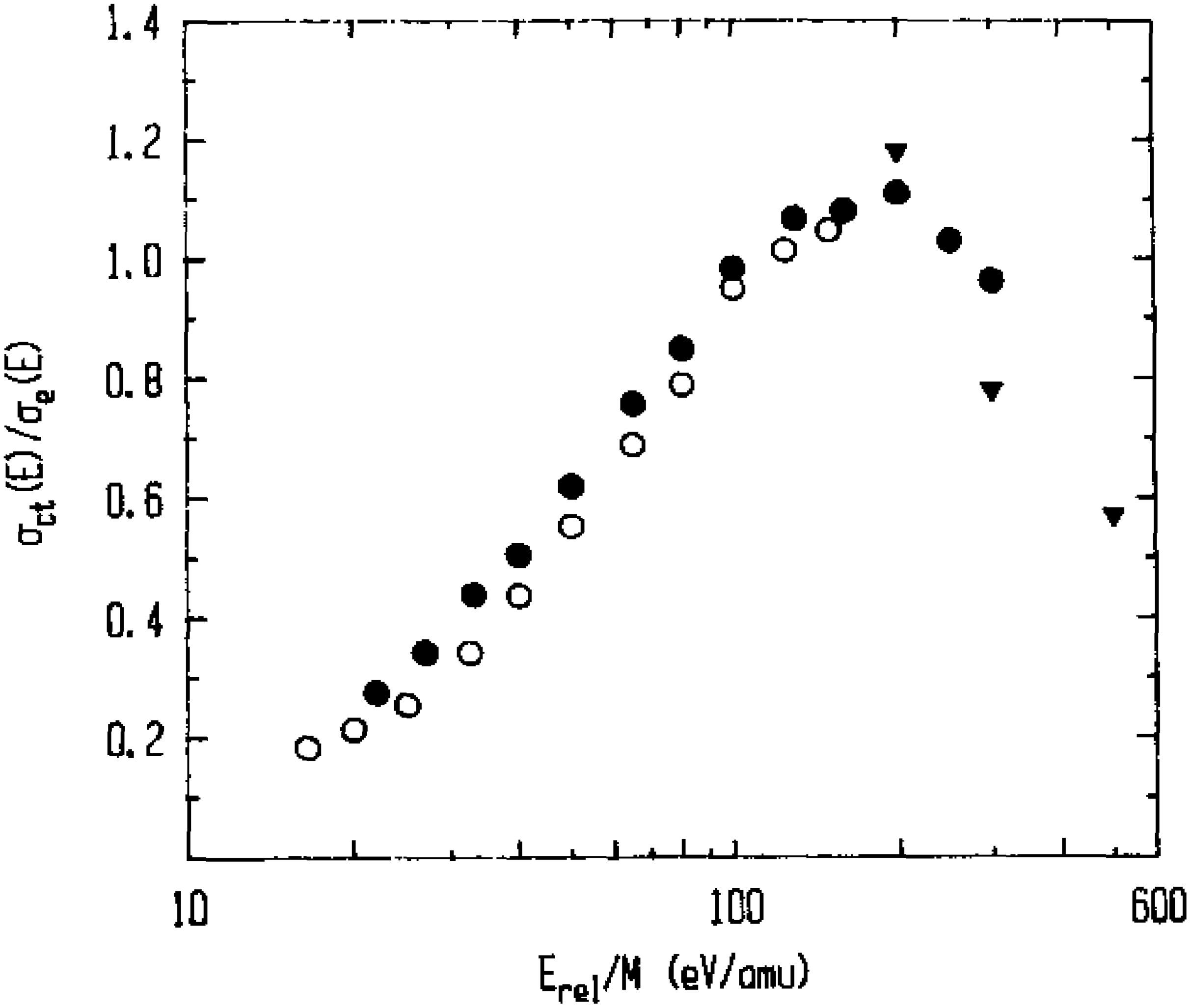

Fig.3.12. Measured ratios, σ_{ct}/σ_e, for H^- + Na (solid circles) and D^- + Na (open circles) versus E_{rel}/M. Solid triangles are the ratios for H^- + Na taken from Ref.35.

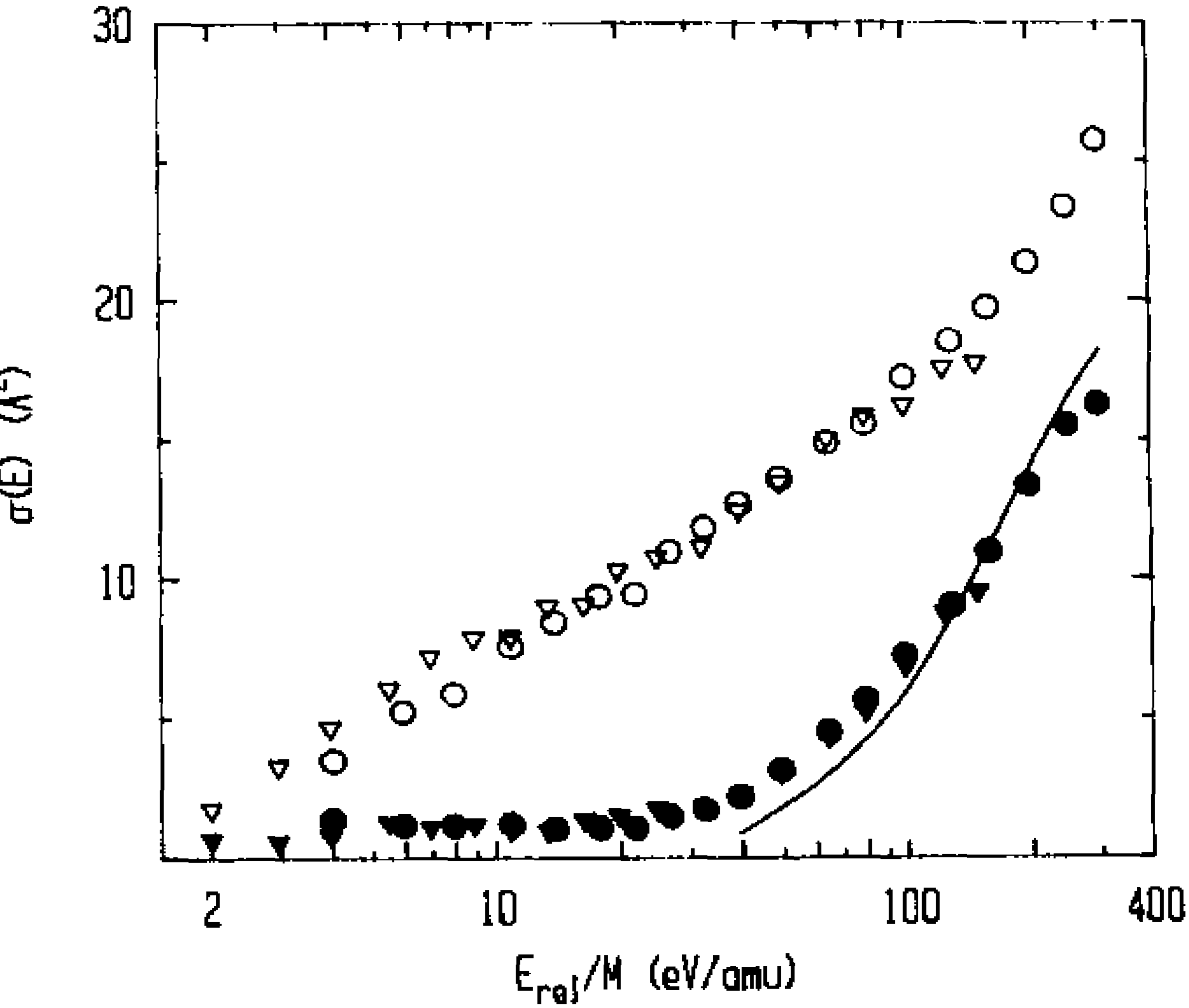

Fig.3.13. Measured σ_{ct} (solid symbols) and σ_e (open symbols) for H^- + K (circles) and D^- + K (triangles) versus E_{rel}/M. Solid line is the calculated σ_{ct} from Ref.33.

TABLE 3.4

$\sigma_{ct}(E)$ and $\sigma_e(E)$ for H^- + K

E_{rel} (eV)	σ_{ct} ($Å^2$)	σ_e ($Å^2$)
3.90	1.38	3.51
5.75	1.21	5.27
7.70	1.18	5.88
10.7	1.22	7.58
13.5	1.06	8.46
17.3	1.08	9.36
21.2	1.07	9.46
25.9	1.49	11.0
31.7	1.74	11.8
38.4	2.19	12.7
48.1	3.15	13.6
62.5	4.53	14.9
76.8	5.64	15.5
96.0	7.24	17.2
125	9.02	18.5
154	11.0	19.7
192	13.3	21.3
240	15.5	23.4
288	16.3	25.8

Note: σ_{ct} are normalized to Olson and Liu's calculation[33] at about E = 150 eV.

TABLE 3.5

$\sigma_{ct}(E)$ and $\sigma_e(E)$ for $D^- + K$

E_{rel} (eV)	σ_{ct} ($\AA^2$)	σ_e ($\AA^2$)
3.81	0.69	1.78
5.61	0.61	3.33
7.52	0.83	4.71
10.4	1.30	6.10
13.1	1.10	7.22
16.8	1.23	7.92
20.6	1.02	7.93
25.3	0.98	9.02
30.9	1.36	9.06
37.5	1.54	10.3
46.9	1.74	10.8
61.0	1.86	11.1
75.0	2.34	12.5
93.7	3.05	13.5
122	4.34	15.0
150	5.25	15.9
188	6.89	16.2
234	8.74	17.6
281	9.53	17.7

Note: the absolute values of σ_{ct} and σ_e for D^- are obtained by normalizing σ_{ct} for H^- to Olson and Liu's calculation[33] about E = 150 eV.

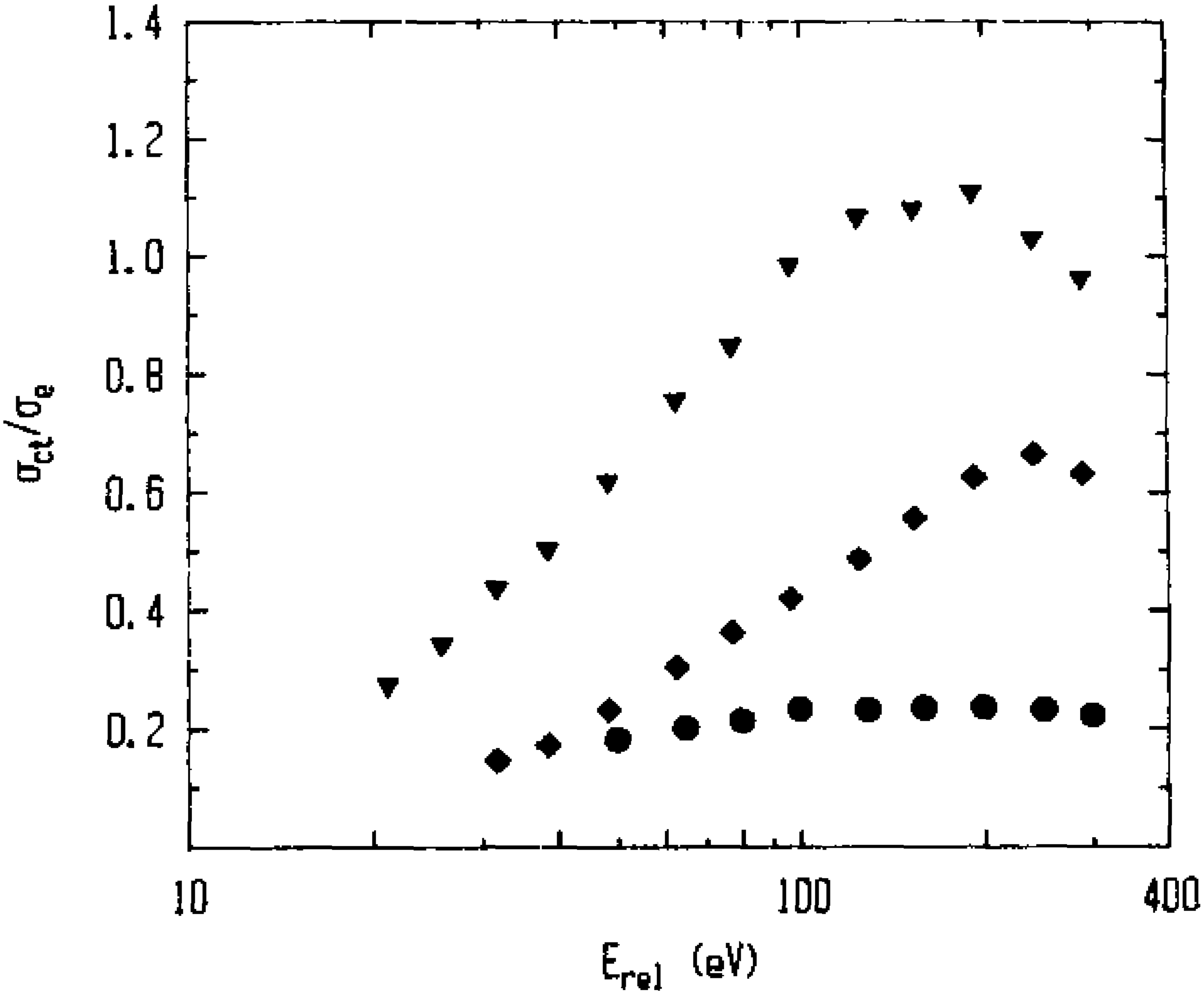

Fig.3.14. Measured ratios, σ_{ct}/σ_e, for H^- + Na (triangles), K (squares) and Cs (circles).

energy. As may be seen in the figure, the general structures of σ_{ct} and σ_e for K are very similar to those for Na. This feature suggests that the electron-loss mechanisms are the same for these two targets. The threshold of σ_{ct} for K is higher than that for Na and the overall cross sections for K are smaller than those for Na. These differences are due to the fact that K has a smaller electron affinity and larger dipole polarizability, and consequently a larger energy gap between the $X^2\Sigma$ and $A^2\Sigma$ states of KH^-.

3.4. $H^-(D^-)$ + Cs

The experimental results for σ_{ct} and σ_e for collisions of H^- and D^- with Cs are shown in Fig.3.15 as functions of E/M, and they are listed in Tables 3.6 and 3.7. Since our measurements overlap the lower collision energy range of the previous measurements of the total electron loss cross sections by Meyer[34] (His results were obtained by monitoring the change in attenuation of the H^- beam due to a change of target length of a Cs vapor cell with known Cs density), they have been normalized to Meyer's results as indicated in Fig.3.15. The ratios σ_{ct}/σ_e for H^- + Cs are shown in Fig.3.14 together with those for H^- + Na and K.

As may be seen, both σ_{ct} and σ_e for $H^-(D^-)$ + Cs, as for Na and K, show a velocity-dependent isotope effect

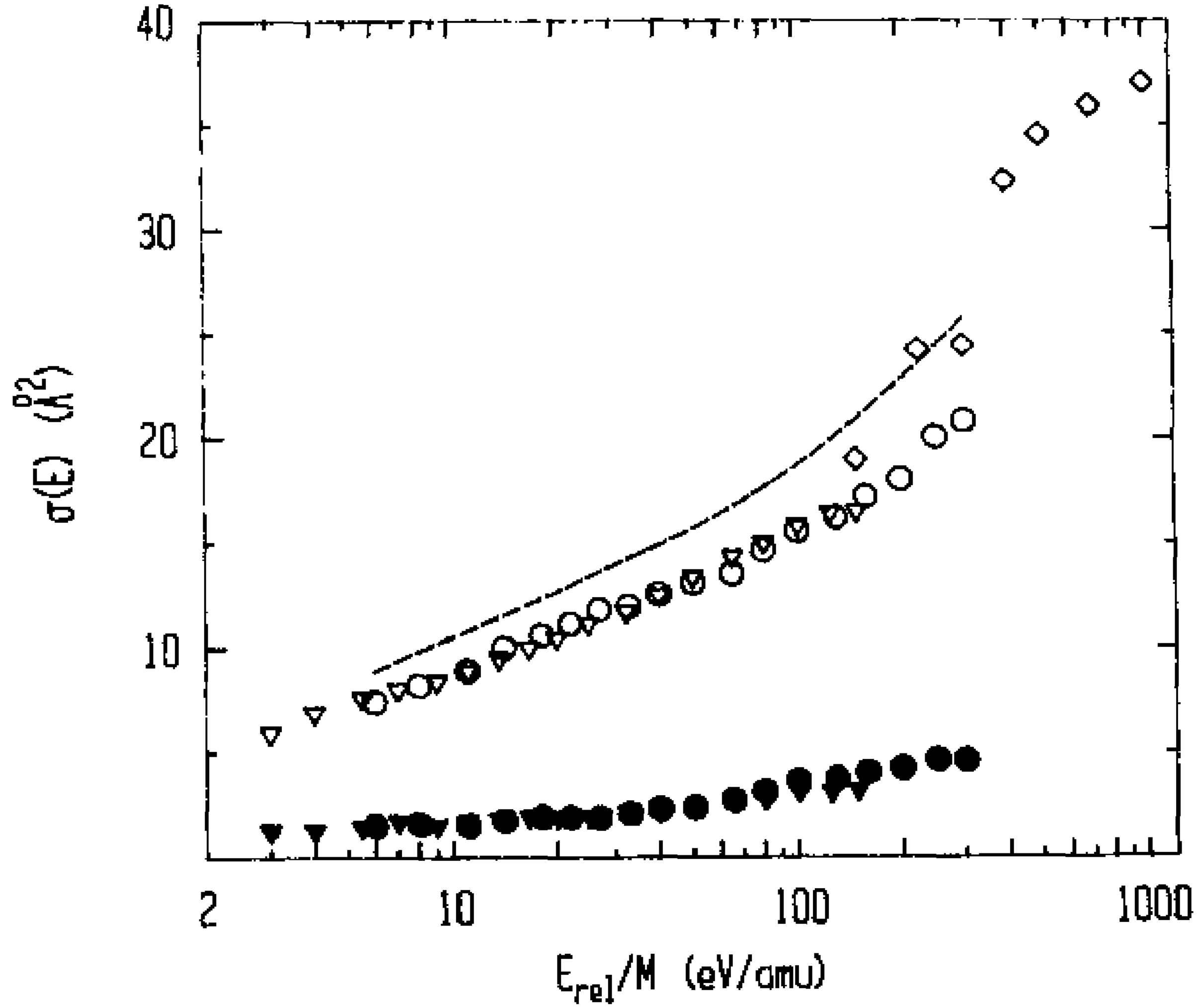

Fig.3.15. Measured σ_{ct} (solid symbols) and σ_e (open symbols) for H^- + Cs (circles) and D^- + Cs (triangles) versus E_{rel}/M, where E_{rel} is the relative collision energy and M the reduced mass of the projectiles. Dashed line is $\sigma_{ct} + \sigma_e$ for H^- + Cs. Open squares are $\sigma_{ct} + \sigma_e$ for H^- + Cs from Ref.34.

TABLE 3.6

$\sigma_{ct}(E)$ and $\sigma_e(E)$ for $H^- + Cs$

E_{rel} (eV)	σ_{ct} ($Å^2$)	σ_e ($Å^2$)
5.96	1.53	7.44
7.94	1.61	8.22
10.9	1.54	8.91
13.9	1.77	10.0
17.9	1.93	10.6
21.8	1.93	11.2
26.8	1.91	11.8
32.8	2.11	12.0
39.7	2.33	12.6
49.6	2.39	13.1
64.5	2.74	13.5
79.4	3.14	14.7
99.3	3.64	15.6
129	3.77	16.2
159	4.05	17.1
199	4.25	18.0
248	4.65	20.0
298	4.63	20.8

Note: the absolute values of σ_{ct} and σ_e are obtained by normalizing $\sigma_{ct} + \sigma_e$ to Meyer's measurements[34] at about $E = 200$ eV.

TABLE 3.7

$\sigma_{ct}(E)$ and $\sigma_e(E)$ for D^- + Cs

E_{rel} (eV)	σ_{ct} ($Å^2$)	σ_e ($Å^2$)
5.91	1.30	5.96
7.88	1.32	6.94
10.8	1.46	7.62
13.8	1.73	8.03
17.7	1.56	8.44
21.7	1.74	8.93
26.6	1.85	9.52
32.5	1.93	10.0
39.4	1.92	10.5
49.3	1.97	11.2
64.0	2.16	11.7
78.8	2.21	12.5
98.5	2.42	13.4
128	2.65	14.4
158	2.81	15.0
197	3.12	15.8
246	3.13	16.4
296	3.22	16.5

Note: the absolute values of σ_{ct} and σ_e for D^- are obtained by normalizing σ_{ct} + σ_e for H^- to Meyer's measurements[34] at about E = 200 eV.

(This isotope effect was also observed in Meyer's earlier measurements). Electron detachment is the dominant electron loss channel; as for the Na and K targets, $\sigma_e(E)$ for H^- + Cs shows a stronger energy dependence at the higher energies than do the H^- + rare-gas systems where electron detachment is explained purely by the coupling between the ionic state and the continuum.[2] This stronger energy dependence suggests that the additional dynamic mechanisms due to the charge exchange coupling are also involved in electron detachment for the H^- + Cs system. The ratios σ_{ct}/σ_e in Fig.3.14 illustrate that the relative importance of charge transfer as an electron-loss mechanism decreases as the mass of the alkali-metal increases. Unlike the results for Na and K, $\sigma_{ct}(E)$ for H^+ + Cs shows no obvious threshold. These features can be understood with the help of a schematic diagram (Fig.3.16) of the potential curves for CsH^- and CsH which are based on the calculations of the ground molecular states of CsH^- and CsH by Karo et al.[32] and the calculations of the low-lying molecular states of NaH^- and NaH by Olson and Liu.[33]

Cs has a larger polarizability than Na; thus the $X^2\Sigma$ state of CsH^- has a stronger long-range attraction potential. This, combined with the smaller electron affinity of Cs, leads to a larger gap between the $X^2\Sigma$ and $A^2\Sigma$ states which consequently reduces their charge exchange coupling. Additionally, the $A^2\Sigma$ state crosses

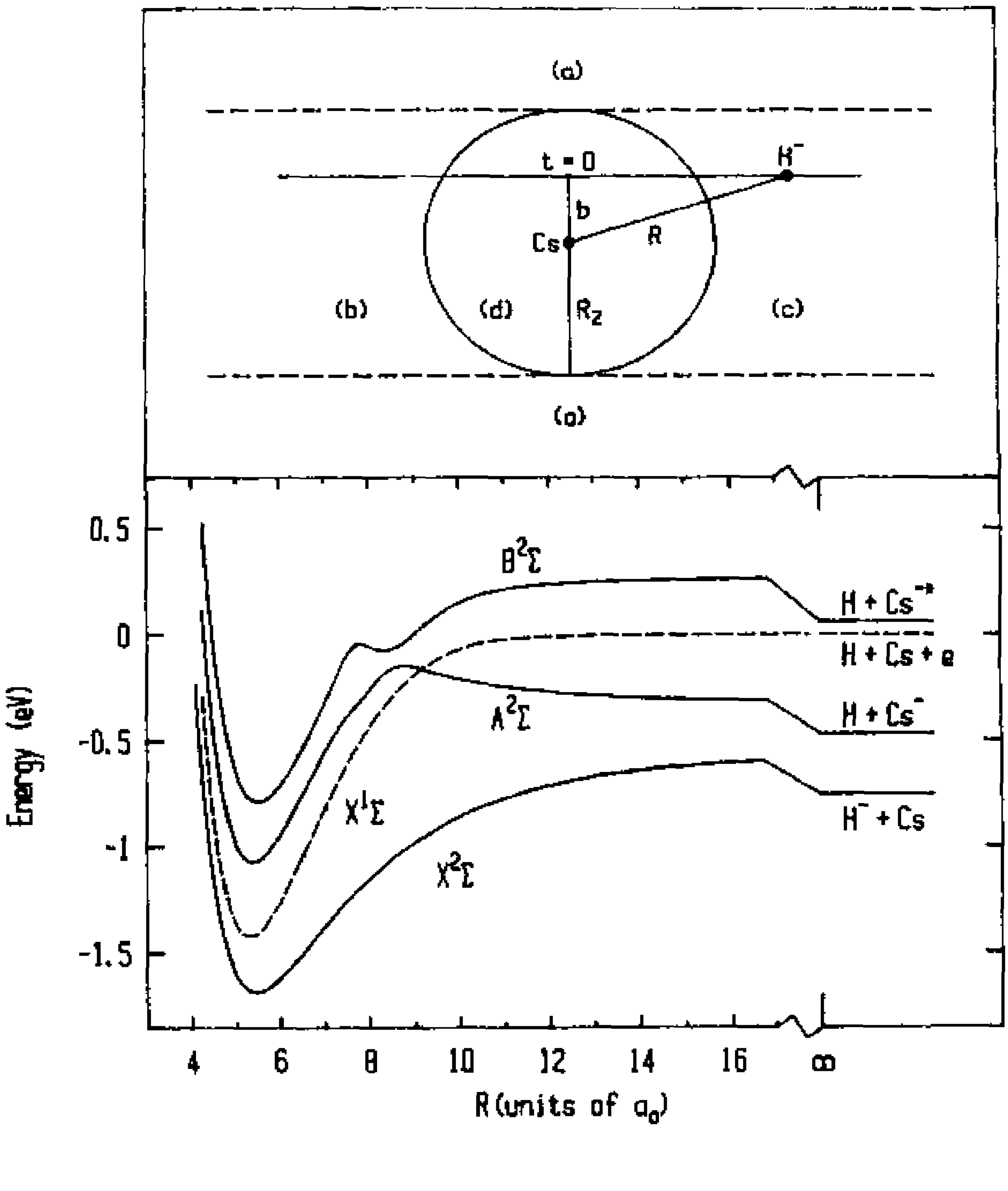

Fig.3.16. Low-lying molecular states of CsH^- (solid lines) and ground state of CsH based on Ref.32 and 33.

into the $X^1\Sigma$ continuum at an internuclear separation R_3 which is larger than the corresponding crossing for the Na target because of the smaller electron affinity of Cs.

As discussed for the H^- + Na system, the key to understanding the collisional dynamics is to identify various effects associated with the $X^2\Sigma$ - $A^2\Sigma$ coupling. To facilitate the following discussion it is helpful to repeat the division of the internuclear separation space:

$$X^2\Sigma - A^2\Sigma \begin{cases} R > R_3 \begin{cases} b > R_3 & \cdots\cdots\cdots\cdots\cdots\cdots \text{(a)} \\ b < R_3 \begin{cases} t > 0 & \cdots\cdots\cdots\cdots \text{(b)} \\ t < 0 & \cdots\cdots\cdots\cdots \text{(c)} \end{cases} \end{cases} \\ R < R_2 \quad \cdots\cdots\cdots\cdots\cdots\cdots\cdots\cdots\cdots\cdots \text{(d)} \end{cases}$$

The meaning of the symbols are the same as given in section 3.2. These regions are illustrated in the inset of Fig.3.16.

The charge transfer is attributed to the $X^2\Sigma$ - $A^2\Sigma$ coupling in regions (a) and (b). For the H^- + Na system, the contribution from region (a) is larger than that from (b). This may no longer be the case for H^- + Cs because of the effectively shorter range of the $X^2\Sigma$ - $A^2\Sigma$ coupling and the larger value of R_3 where the $A^2\Sigma$ state crosses into the $X^1\Sigma$ continuum. The coupling in (b) is responsible for a larger fraction of the total charge transfer cross section at low energy because the "effective radius" of the coupling decreases when the impact velocity decreases. This relative importance of the coupling in (b) perhaps is the principal reason why $\sigma_{ct}(E)$ for Cs has a threshold behavior different from those for Na and K. The shorter $X^2\Sigma$ - $A^2\Sigma$ coupling and the larger R_3 for a heavier alkali-metal target also determines the trend that the relative importance of charge transfer as an electron-loss mechanism decreases as the mass of the alkali-metal increases.

The electron detachment in collisions of H^- + Cs is attributed to the possible curve crossing between the $X^2\Sigma$ state and the $X^1\Sigma$ continuum and the $X^2\Sigma$ - $A^2\Sigma$ coupling in regions (c) and (d), as for the H^- + Na system. The crossing point between the $X^2\Sigma$ state and the $X^1\Sigma$ continuum is not precisely known; however the molecular potential curves of CsH^- and CsH presented by Karo et al.[32] suggest that a crossing between $X^2\Sigma$ and $X^1\Sigma$ is likely at an internuclear separation, $R < 4\ a_o$. This curve-crossing mechanism is expected to be weakly energy dependent at high energy.[2] In comparison to the H^- + Na, the $X^2\Sigma$ - $A^2\Sigma$ coupling for H^- + Cs in region (d) becomes more important than that in (c) in leading to electron detachment because of the shorter $X^2\Sigma$ - $A^2\Sigma$ coupling and the larger R_3. This coupling in (d) will be strongly energy dependent because of the near-resonant nature of these two states.[22]

It should be mentioned that Olson and Liu's estimates for charge transfer and electron detachment cross sections in the H^- + Cs collisions fails to agree with the present measurements. Their calculated electron detachment cross section is thought to fail for the same reasons as discussed for the H^- + Na system. Their charge transfer at 300 eV is approximately double the measured value. Their two-states PSS calculations for a different alkali-metal target apparently took into account only the different energy gap between the corresponding diabatic potentials, and they were performed by assuming that the diabatic coupling term and the $A^2\Sigma$ - $X^1\Sigma$ crossing were the same as for H^- + Na. The so-assumed $A^2\Sigma$ - $X^1\Sigma$ crossing may significantly deviate from reality since the equilibrium separation for CsH is larger than that for NaH by about 1 a_0.

The exact internuclear separation, R_3, where the $A^2\Sigma$ state crosses into the $X^1\Sigma$ continuum for these systems could be investigated by observing the electron detachment cross sections in collisions of alkali-metal negative ion with hydrogen. The direct detachment due to the $A^2\Sigma$ - $X^1\Sigma$ crossing in such collisions is obviously the dominant electron detachment channel and it will yield a near constant cross section $\pi R_3{}^2$ above energetic threshold.

In summary, electron detachment is the dominant electron-loss channel in slow collisions of H^- and D^- with Cs; charge transfer is less important for Cs than for Na and K. Both processes exhibit velocity-dependent isotope effects for H^- and D^-; i.e., the cross sections are equal at comparable values of E/M. The observed isotope effects are consistent with the two-state PSS model for such collisions.

Chapter 4

SUMMARY AND THOUGHTS FOR FURTHER WORK

The cross sections of charge transfer and electron detachment in collisions of H^- and D^- with Na, K and Cs have been measured for collision energies ranging from 3 to 300 eV. Both charge transfer and electron detachment are significant electron-loss mechanisms for $H^-(D^-)$; both processes exhibit velocity-dependent isotope effects for $H^-$and D^-. $\sigma_{ct}(E)$ displays high energetic thresholds for Na and K (about 20 eV for H^- + Na and 40 eV for H^- + K) yet no obvious one for Cs. $\sigma_e(E)$ does not depend on the target as much as $\sigma_{ct}(E)$ and displays near zero-energy thresholds. The relative importance of charge transfer as an electron-loss mechanism decreases as the mass of the alkali-metal increases.

The crossed-beam apparatus has been tested, modified and proved to be in good working condition. Alkali-metal target beams are readily available now in this laboratory and can be used for future studies such as Na^- + Na and K^- + Na, etc. No doubt, studies of these resonance or near-resonance reactions will significantly increase our understanding of negative-ion collisions.

In the following sections, I will describe a few thoughts which are closely related to the work described in this dissertation.

4.1. $Na^- + H$

Cross section measurements of charge transfer and electron detachment in $Na^- + H$ (e.g., an H beam produced in a RF-discharge atomic source) collisions will be complementary to the results obtained for the $H^- + Na$ collisions (this is also true for K and Cs). The absolute values of the cross sections for $H^- + Na$ were not determined in the present crossed-beam experiments, so the experimental results were normalized to a theoretical calculation. For $Na^- + H$, however, the absolute value of the cross sections can be obtained because one can determine the H-target thickness by turning-off the power to the atomic source and measuring the cross sections for $Na^- + H_2$ which has been studied previously in this laboratory. The PSS calculation for

$$H^- + Na = H + Na^-$$

is reversible for a given trajectory, and thus the charge transfer cross sections for $Na^- + H$ collisions can be calculated with the same method used for $H^- + Na$. A comparison between such a calculation and the measured $\sigma_{ct}(E)$ for $Na^- + H$ will clarify the normalization used for $H^- + Na$.

4.2. Negative Ion Production on a Metallic Surface

It is found in the alkali-metal target experiments that some negative ions desorb from alkali-coated surfaces, and this process increases dramatically when the partial pressure of oxygen increases. Are these negative ions O^- or O_2^-? This question can be easily answered by mass analysis. It is not so easy, however, to understand the production mechanism for either negative ion. If we assume that the surface can be described by a single parameter —— its work function (the work functions for Na, K and Cs are 2.35, 2.22 and 1.81 eV, respectively. They may decrease significantly due to the presence of oxygen), the negative-ion formation can possibly be due to a charge transfer process between the surface and O or O_2. For O_2^- formation, the energy defect is large (the electron affinity of O_2 is about 0.5 eV); where may the extra energy come from? For O^-, the energy defect could be small, and thus O^- appears to be favored. However the production of O itself relies on other processes on the surface such as

$$2Na + O_2 \rightarrow Na_2O + O$$

which is endothermic. Thermal energy probably plays some role in either negative ion formation. A very interesting set of experiments would be to measure the negative ion production, along with the kinetic energy distribution, at different temperatures and work functions of the surface.

4.3. Electron Detachment and EPR Paradox

The paradox of Einstein, Podolsky and Rosen[41] (EPR) envisions a hypothetical experiment on a system of two particles which are position and momentum correlated. Their proposal suggested certain apparently paradoxical predictions of quantum mechanics. A conceptually equivalent but simpler example of the EPR experiment due to Bohm[42,43] is a spin-zero system which consists of two spin-1/2 particles. In order to illustrate the EPR paradox and its relation to the electron detachment process in H^- + Na (the same for other alkali-metal targets) collisions, let us first examine the spin rearrangements in collisional electron detachment

$$H^- + Na \rightarrow H + Na + e.$$

H^- is a spin-zero system and the two electrons in H^- are spin correlated before the collision, while H and Na atoms (both spin-1/2) are spin correlated and H + Na as a whole is a spin-zero system after the collision because electron detachment in low energy collisions is caused mainly by the $X^2\Sigma$ - $X^1\Sigma$ and $A^2\Sigma$ - $X^1\Sigma$ couplings, i.e., the quasi-molecule H + Na is produced in the singlet $X^1\Sigma$ state. The spin wavefunction for such a spin-zero system is

$$1/2^{1/2} \left(|\uparrow\rangle_1 |\downarrow\rangle_2 - |\downarrow\rangle_1 |\uparrow\rangle_2 \right), \qquad (4.1)$$

where the reference axis for spin-up $\uparrow$ and spin-down $\downarrow$ is arbitrary and can be in any desired direction. Each particle in the system has equal probability for spin-up or spin-down. However, the zero total spin means that if the spin-component of one of the particles is measured, the same spin-component of the other particle can be immediately known to be in the opposite direction. In other words, the measurement reduces the wavefunction (4.1) to $|\uparrow\rangle_1 |\downarrow\rangle_2$ or $|\downarrow\rangle_1 |\uparrow\rangle_2$. If such "instantaneous change" of the wavefuntion is acceptable when the two particles are strongly interacting, such as the two electrons in H^-, it is very paradoxical when the two particles are arbitrarily far apart such as the H + Na system after a detachment collision. In such circumstances, how can the spin of one particle "follow" that of the other? Does the instantaneous reduction of the wavefunction represent a real phenomenon, or is it merely a linguistic defect confined to the formalism which describes the system?

Einstein[44] considered quantum mechanics incomplete or defective and believed that reality is local (no communication faster than the speed of light) and predetermined (reality has definite physical attributes which exist independent of human observation). The EPR paradox, when applied to the H + Na system, is as follows: After H and Na have separated far enough so that they cease to interact, the spin-component of one particle, say Na, is measured along a desired reference axis. Since such an axis can be chosen arbitrarily, one can predict, based upon the spin measurement on Na, the spin-component of H with respect to any direction without disturbing H (locality); thus the spin-components of H must have been determined beforehand (determinism, in the sense that the spin-components of Na or H are considered to be elements of reality before they are measured). This much information is not, however, included in the quantum-mechanical wavefunction and thus quantum mechanics is "incomplete."

This so-called "incompleteness" in quantum mechanics has led to extensive efforts to find additional (or "hidden") variables describing a quantum system such that when they are specified, the outcome of any measurement can be predicted with certainty.

An important clarification of the EPR paradox was made by Bell[45] in 1964. Bell's theorem states that for the description of an EPR-type experiment, no local hidden variable theory is consistent with quantum mechanics. Bell's theory is in the form of an inequality that must be satisfied if local hidden variables underlie the system. Quantum-mechanical predictions do not satisfy the inequality. An elementary derivation of Bell's inequality due to Herbert[46] will be presented here in order to illustrate the theorem.

Suppose that the spin-correlated H and Na have flown far apart, and that we know the paths along which the H and Na atoms travel, and that the spin-components of H and Na are measured with H and Na detectors, respectively. Each coincidence is then recorded in a pair of "binary messages" according to the following scheme: Let the message bit at the H detector be "1" if H is detected in the spin-up state; call it "0" if H is spin-down. The contrary convention is chosen for the Na detector. When two detector axes are aligned, because of the spin correlation of H and Na, message streams recorded at the two detectors are identical [Fig.4.1(a)].

Suppose that the axis of the Na detector is mis-aligned by an angle δ. Then some bits in the two message streams will not be the same; these "missed" bits appear-ing in an unit of time are interprated as an error rate $n(\delta)$ in the message stream at the Na detector [Fig.4.1(b)]. If now the H detector is turned by the same amount δ [Fig.4.1(c)], the same error rate is introduced into the H message stream. Moreover the "errors" fall at precisely the correct places in the H message stream to make the two messages again coincide.

Now, we suppose that the H detector is turned by δ in the opposite direction from that of the Na detector such

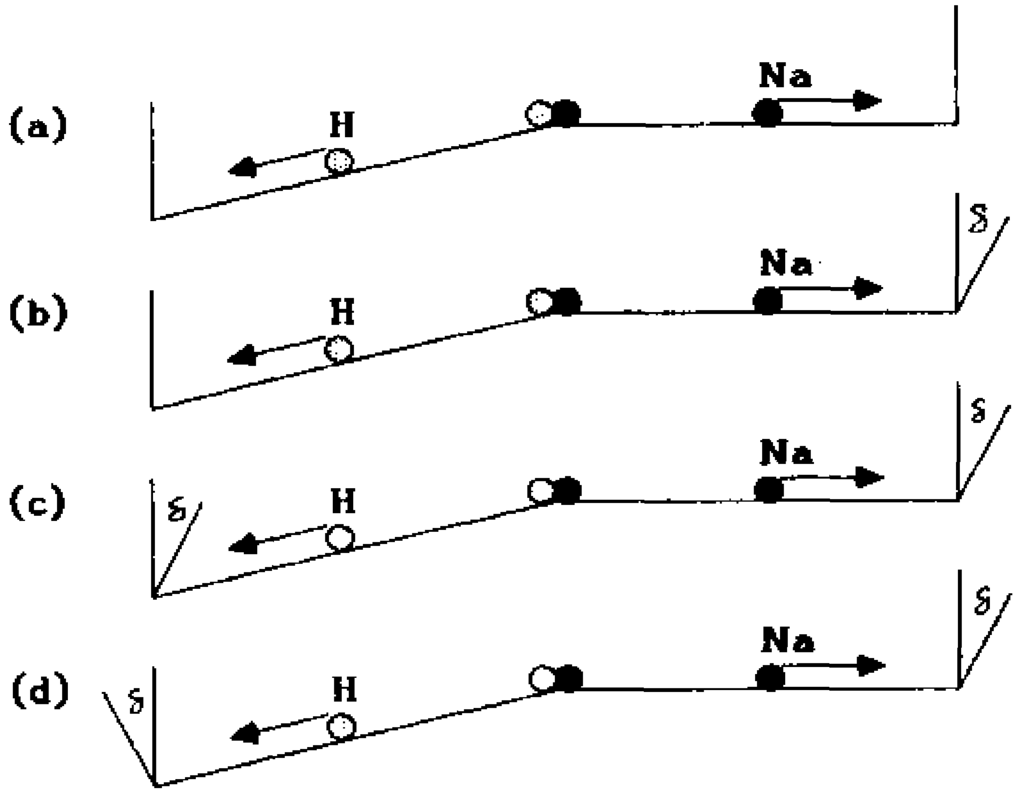

Fig.4.1. Special alignments of spin-detection system: (a) perfect alignment; (b) Na detector is turned by δ; (c) both detectors are turned by δ in the same direction; (d) both detectors are turned by δ but in opposite directions.

that the new misalignment between the two detectors is 2δ [Fig.4.1(d)]. What is the new error rate $n(2\delta)$?

If reality is local, i.e., changes in the message stream of one atom depend only upon changes in the setting of its corresponding detector, not on the position of the other detector, a change δ in alignment always introduces errors $n(\delta)$. But in two successive misalignments, some of these errors may cancel so $n(2\delta)$ can never be greater than $2n(\delta)$

$$n(2\delta) \leq 2n(\delta). \tag{4.2}$$

Equation (4.2) is a special case of Bell's inequality.

The derivation of the quantum-mechanical prediction for the error rate $n(\delta)$ in the above experiment is straightforward. Suppose the spin-component of one particle, say Na, is detected in the spin-up state, then the spin-wavefunction of the system after detection is $|\uparrow\rangle_{Na}|\downarrow\rangle_H$ and the spin-component of H has a probability of $\cos^2(\delta/2)$ to be in the spin-down state along the misaligned axis. Thus the error rate $n(\delta)$ is

$$n(\delta) = 1 - \cos^2(\delta/2) \tag{4.3}$$

The quantum-mechanical prediction (4.3) violates the Bell's inequality (4.2), e.g., $n(2\delta) = 0.25 > 2n(\delta) \approx 0.13$ at $\delta = \pi/6$. This contradiction enables experimental tests of the EPR paradox by measuring the ratio of the error rates, $n(2\delta)/n(\delta)$. Bell's inequality gives an upper limit of 2 for this ratio, while quantum mechanics predicts that the ratio is $4\cos^2(\delta/2)$ which is larger than 2 for all $\delta < \pi/4$.

A number of experiments have been performed to test Bell's inequality; these have been reviewed in several articles.[47,48] Most of the experiments involve a spin-zero system of two correlated photons, and they can be categorized according to the photon sources: (1) low-energy correlated photons produced in an atomic cascade such as the $(4s6s)^1S_0 \rightarrow (4s4p)^1P_1 \rightarrow (4s^2)^1S_0$ cascade in a calcium atom; (2) high-energy correlated γ rays emitted during annihilation of a particle-antiparticle system such as electron-positron. The only experiment performed thus far which involved particles with a finite rest mass is a 13 MeV proton-proton scattering experiment.[49]

The experimental evidence for a violation of Bell's inequality and consequently a rejection of local hidden-variable theories appears to be overwhelming.[47,48] However, arguments still exist and it can not yet be said that the EPR paradox has been totally resolved not only because there have been a few experiments which agreed with Bell's inequality, but also because there are loopholes in explaining those experiments whose results violate Bell's inequality. For the photon experiments the loopholes are due to: (1) lack of detection efficiency ——

highly efficient polarization analyzers can be achieved only for low-energy photons, while highly efficient detectors can be made only for high-energy photons; (2) large "dimensions" of photons —— the coherent length of the γ rays is about 17 cm and the length of the atomic photons is about 300 cm (both are comparable to the dimensions of the apparatus used and therefore it is not clear that locality is respected). The proton-proton experiment[49] has the apparent defect of the low efficiency of the polarization analysis.

The experimental tests of the EPR paradox using a spin-zero system of two correlated spin-1/2 atoms, such as the H + Na system, have been long preferred and hoped by physicists.[42-50] The problems which plague the photon experiments can, in principle, be overcome with this atomic system. The interaction between the two atoms can be considered zero when the separation between them is of macroscopic order. Spin analysis of a neutral atom can be done with a Stern-Gerlach magnet having virtually 100% transmission. Na can be detected by ionization on a hot surface while H can be detected by a conventional electron multiplier, with both detection efficiencies being nearly 100%.

The reason why the preferred experiments have not been done is not very clear to me. Here I will cite the views of several experts in this field. In their review of the EPR paradox, Bohm and Aharonov[43] said in 1957: "We consider a molecule of spin zero consisting of two atoms, each of spin one-half. ...... The two atoms are then separated by a method that does not influence the total spin." Clauser et al.[50], in their proposal of the photon experiment to test Bell's inequality, wrote in 1969: "Bohm's Gedankenexperiment, involving correlated spin-1/2 particles, has not been performed, nor does it appear to be easily realizable." Later in 1978, in their review of about a dozen experimental tests of Bell's theorem, Clauser and Shimony[47] stated: "There is hope that the requirement for efficient analysis and detection can be achieved by observing the dissociation fragments of a metastable molecule, ...".

It appears that the door is still open for an "invention" to make spin-correlated atoms. Generally speaking, the electron detachment process in the low-energy collision of a spin-zero negative ion with a spin-1/2 atom could provide possibly one of the best ways to produce spin-correlated atoms. The possible candidates, in addition to H^- + Na, include D^- + Na, Li^- + Na and Cl^- + K. Another ather different way to make spin-correlated atoms is low-energy neutral-neutral elastic atomic collisions such as Cl + Na; Cl and Na will be mainly in the spin-zero state when they emerge in the direction of the classical rainbow angle. A more detailed analysis of technical aspects is required to determine which approach outlined above is better.

Appendix A

EXCHANGE CORRELATION IN H^-

For the hydrogen negative ion, the system Hamiltonian is

$$H = h_1 + h_2 + \frac{1}{r_{12}}$$

with the single-electron Hamiltonian being

$$h = -\frac{1}{2}\nabla^2 - \frac{1}{r}$$

where

$$\nabla^2 = \frac{1}{r^2}\frac{\partial}{\partial r}\left(r^2\frac{\partial}{\partial r}\right) - \frac{\hat{L}^2}{r^2} \quad .$$

To examine the importance and nature of the correlation effect in leading to the stable negative ion, we now compare the result obtained for the total energy of the system, using the trial function

$$\phi(r_1,r_2) = \frac{\alpha^{3/2}}{\pi}\exp(-r_1-\alpha r_2)$$

which includes no correlation, with the result using

$$\Psi(r_1,r_2) = \left(\frac{\alpha^3}{2\pi^2}\right)^{½}\left[\exp(-r_1-\alpha r_2) + \exp(-r_2-\alpha r_1)\right]$$

$$= 1/2^{½}\left[\phi(r_1,r_2) + \phi(r_2,r_1)\right]$$

which includes correlation. The atomic units will be used in this appendix.

For trial function ϕ, we have

$$<\phi|\nabla_1^2|\phi> = \frac{\alpha^3}{\pi^2}\int_0^\infty \exp(-2\alpha r_2)\ 4\pi r_2^2\ dr_2$$

$$\times\int_0^\infty \exp(-r_1)\ [\nabla_1^2\ \exp(-r_1)]\ 4\pi r_1^2\ dr_1$$

$$= -1$$

and likewise, we can get

$$<\phi|\frac{1}{r_1}|\phi> = 1\ ,$$

$$<\phi|\nabla_2^2|\phi> = -\alpha^2$$

and $$<\phi|\frac{1}{r_2}|\phi> = \alpha\ .$$

To determine the repulsion energy between two electrons, we will first evaluate the average potential at r_2 due to the electron 1,

$$U(r_2) = \int_0^\infty \frac{1}{r_{12}}\ \exp(-2r_1)\ 4\pi r_1^2\ dr_1$$

$$= (\int_0^{r_2}\frac{1}{r_2} + \int_{r_2}^\infty \frac{1}{r_1})\ \exp(-2r_1)\ 4\pi r_1^2\ dr_1\ .$$

The first term in the above integral is

$$\int_0^{r_2}\frac{1}{r_2}\ \exp(-2r_1)\ 4\pi r_1^2\ dr_1 = \frac{\pi}{2r_2}\int_0^{2r_2} \exp(-t)\ t^2\ dt$$

$$= \frac{\pi}{r_2} \left[1 - (1 + 2r_2 + 2r_2^2) \exp(-2r_2)\right]$$

and the second term is

$$\int_{r_2}^{\infty} \frac{1}{r_1} \exp(-2r_1)\ 4\pi r_1^2\ dr_1 = \pi\ (1 + 2r_2) \exp(-2r_2) \ .$$

Thus we have

$$U(r_2) = \frac{\pi}{r_2} \left[1 - (1 + r_2) \exp(-2r_2)\right] \ .$$

The repulsion energy between the two electrons is

$$<\phi|\frac{1}{r_{12}}|\phi> = \frac{\alpha^3}{\pi^2} \int_o^{\infty} U(r_2) \exp(-2\alpha r_2)\ 4\pi r_2^2\ dr_2$$

$$= \alpha - \frac{\alpha^3(2+\alpha)}{(1+\alpha)^3} \ .$$

Finally we have the total energy of the system

$$E(\alpha) = -\frac{1}{2} + \frac{\alpha^2}{2} - \frac{\alpha^3(2+\alpha)}{(1+\alpha)^3}$$

which yields the minimum at $\alpha = 0$ and

$$E_{min} = -1/2 \ .$$

This minimum energy equals to the ground energy of a neutral hydrogen atom. Thus the trial function ϕ which includes no correlation fails to predict the stability of H^-.

For trial function Ψ, we have

$$<\Psi|H|\Psi> = <\phi(r_1,r_2)|H|\phi(r_1,r_2)> + <\phi(r_1,r_2)|H|\phi(r_2,r_1)>$$

The first term in the above formula has the same expression as the total energy for the trial function ϕ, and we need to calculate the second term only. We have followings:

$$\langle\phi(r_1,r_2)|\nabla_1^2|\phi(r_2,r_1)\rangle = \langle\phi(r_1,r_2)|\nabla_2^2|\phi(r_2,r_1)\rangle$$

$$= \frac{\alpha^3}{\pi^2}\int_o^\infty \exp[-(1+\alpha)r_1]\ 4\pi r_1^2\ dr_1$$

$$\times \int_o^\infty \exp(-\alpha r_2)\ [\nabla_2^2 \exp(-r_2)]\ 4\pi r_2^2\ dr_2$$

$$= -\frac{64\alpha^4}{(1+\alpha)^6},$$

$$\langle\phi(r_1,r_2)|\frac{1}{r_1}|\phi(r_2,r_1)\rangle = \langle\phi(r_1,r_2)|\frac{1}{r_2}|\phi(r_2,r_1)\rangle$$

$$= \frac{32\alpha^3}{(1+\alpha)^5}.$$

$$U(r_2) = \int_o^\infty \frac{1}{r_{12}} \exp[-(1+\alpha)r_1]\ 4\pi r_1^2\ dr_1$$

$$= \frac{4\pi}{(1+\alpha)^3 r_2}\ \{2 - [2 + (1+\alpha)r_2]\ \exp[-(1+\alpha)r_2]\}$$

and

$$\langle\phi(r_1,r_2)|\frac{1}{r_{12}}|\phi(r_2,r_1)\rangle$$

$$= \frac{\alpha^3}{\pi^2}\int_o^\infty U(r_2)\ \exp[-(1+\alpha)r_2]\ 4\pi r_2^2\ dr_2$$

$$= \frac{20\alpha^3}{(1+\alpha)^5} .$$

The trial function Ψ is not normalized, and

$$\langle\Psi|\Psi\rangle = \langle\phi(r_1,r_2)|\phi(r_1,r_2)\rangle + \langle\phi(r_1,r_2)|\phi(r_2,r_1)\rangle$$

$$= 1 + \frac{64\alpha^3}{(1+\alpha)^6} .$$

The total energy of the system is

$$E(\alpha) = -\frac{(1-\alpha)(1+\alpha)^7 + 2\alpha^3(2+\alpha)(1+\alpha)^3 + 8\alpha^3(11-5\alpha)}{2(1+\alpha)^6 + 128\alpha^3} .$$

Its minimum is numerically found at about $\alpha = 0.28$ and

$$E_{min} \approx -0.513 .$$

This minimum energy is less than the bound energy of the ground hydrogen atom; thus the trial function Ψ which includes the exchange correlation predicts the stability of H^-.

Appendix B

DIMER FRACTIONS IN ALKALI-METAL VAPORS

For general multi-component systems, the first law of thermodynamics (the law of conservation of energy) can be written in the form

$$dE = TdS - pdV + \mu_i dN_i \qquad (B.1)$$

where N_i is the number of moles of component i and

$$\mu_i = \partial E/\partial N_i$$

is called the chemical potential. If we subtract d(TS) from both sides of Eq.B.1, we get

$$dF = -SdT - pdV + \mu_i dN_i$$

where $F = E - TS$ is called the Helmholtz free energy. With this alternative form of the first law, we have a new expression for the chemical potential

$$\mu_i = \partial F/\partial N_i$$

The Helmholtz free energy F is related to the partition function Q by

$$F = - kT \ln Q$$

In a mixture of ideal gases, the species are independent and distinguishable, and so the partition function of the mixture is a product of the partition functions of the individual components. Thus

$$Q = \prod_i q_i^{N_i}/N_i!$$

The chemical potential of each species is given by

$$\mu_i = -kT\ \partial \ln Q/\partial N_i = -kT\ \ln(q_i/N_i)$$

where Sterling's approximation $\ln N! = N\ln N - N$ has been used.

The second law of thermodynamics, when applied to a system at equilibrium, yields $dF = 0$. For the reaction

$$2A \rightleftharpoons A_2$$

at equilibrium under fixed T and V, we have

$$dF = \mu_1 dN_1 + \mu_2 dN_2 = 0$$

where subscript 1 is for the atom and 2 for the dimer. Additionally, conservation of atoms requires that

$$dN_1 + 2dN_2 = 0$$

This reduces the equilibrium condition to

$$2\mu_1 = \mu_2$$

or

$$\frac{p_2}{p_1^2} = \frac{V}{kT}\frac{q_2}{q_1^2} \tag{B.2}$$

The partition function for the monatomic gas

$$q_1 = q_{trans}\, q_{ele}$$

with q_{trans} being translational partition function

$$q_{trans} = (2\pi m_1 kT/h^2)^{3/2}\, V$$

and q_{ele} being the electronic partition function which is taken to be the degeneracy of the ground state of the atom at low temperature (such that the first excited state is not involved in the reaction). The partition function for the diatomic gas

$$q_2 = q_{trans}\, q_{rot}\, q_{vib}\, q_{ele}$$

where q_{trans} has the same expression for the monatomic gas except the mass, and the rotational partition function q_{rot} is approximately

$$q_{rot} = \frac{T}{2\Theta_r}$$

where Θ_r is the characteristic temperature of rotation, and the vibrational partition function q_{vib} is

$$q_{vib} = \frac{e^{-\beta h\nu/2}}{1 - e^{-\beta h\nu}}$$

and the electronic partition function q_{ele} is

$$q_{ele} = \exp(\beta D_e).$$

With the above information of partition functions, we can rewrite Eq.B.2

$$\frac{p_2}{p_1^2} = \frac{1}{4kT}\left(\frac{h^2}{\pi m_1 kT}\right)^{3/2}\frac{T}{2\theta_r}\frac{\exp(D_o/kT)}{1-\exp(-\theta_v/T)} \qquad (B.3)$$

The related molecular constants for hydrogen and alkali-metals are listed in table B.1.

TABLE B.1

Melocular Constants of the First Group Elements

Molecule	D_o (eV)	θ_v (K)	θ_r (K)
H_2	4.4781	6332.4	87.555
Li_2	1.046	505.63	0.9678
Na_2	0.720	228.95	0.2226
K_2	0.514	132.40	0.0816
Rb_2	0.49	82.457	
Cs_2	0.394	60.461	0.0183

Note: the data in this table are taken from Ref.51.

The equation B.3, combined with the equation of the saturation pressure of the vapor (p_1 is taken to be the saturation pressure, to the first order) is used to estimate the fractions of the dimers which are shown in Fig.2.4.

References

1. R. L. Champion, L. D. Doverspike, and S. K. Lam, Phys. Rev. A <u>13</u>, 617 (1976).

2. R. L. Champion, Adv. Electron. Electron Phys. 58, <u>143</u> (1982).

3. L. I. Schiff, <u>Quantum Mechanics</u>, 3rd edition (McGraw-Hill, New York, 1968), p84.

4. H. Massey, <u>Negative Ions</u>, 3rd edition (Cambridge University Press, London, 1976).

5. J. E. Hart and G. Herzberg, Phys. Rev. <u>106</u>, 79 (1957).

6. D. Feldmann, in <u>Abstracts of Papers of the IXth International Conference on the Physics of Electronic and Atomic Collisions, Seattle, 1975</u>, p922.

7. A. Kasdan and W. C. Lineberg_r, Phys. Rev. A <u>10</u>, 1658 (1974).

8. J. Slater et al, in <u>Abstracts of Papers of the Xth International Conference on the Physics of Electronic and Atomic Collisions, Paris, 1977</u>, p1172.

9. J. Slater et al, Phys. Rev. A <u>17</u>, 201 (1978).

10. D. Feldmann, Chem. Phys. Lett. <u>47</u>, 338 (1977).

11. Ya. M. Fogel', V. F. Kozlov and A. A. Kalmykov, Zh. Eksp. Teor. Fiz. <u>36</u>, 1954 (1959).

12. L. M. Branscomb et al, Phys. Rev. <u>111</u>, 504 (1958).

13. R. S. Berry et al, J. Chem. Phys. <u>49</u>, 127 (1968).

14. G. Pietsch and L. Rehder, Z. Naturforsch. A <u>22</u>, 2127 (1967).

15. R. Milstein and R. S. Berry, J. Chem. Phys. <u>55</u>, 4146 (1971).

16. L.G. Christophorou, editor, <u>Electron-Molecule Interactions and Their Applications</u> (Academic, New York, 1984).

17. A. J. Deutsch, Rev. Mod. Phys. 20, 388 (1948).

18. R. Wildt, Astrophys. J. 89, 295 (1939).

19. J. R. Hiskes, A. M. Karo, and M. A. Gardner, J. Appl. Phys. 47, 3888 (1976).

20. S. K. Lam, J. B. Delos, R. L. Champion, and L. D. Doverspike, Phys. Rev. A 9, 1828 (1974).

21. R. E. Olson and B. Liu, Phys. Rev. A 22, 1389 (1980).

22. J. P. Gauyacq, J. Phys. B 13, 4417 (1980).

23. J. P. Gauyacq, J. Phys. B 13, L501 (1980).

24. R. D. Taylor and J. B. Delos, Proc. R. Soc. London, A 379, 179 (1982).

25. R. D. Taylor and J. B. Delos, Proc. R. Soc. London, A 379, 209 (1982).

26. T.S. Wang and J.B. Delos, J. Chem. Phys. 79, 4306 (1983).

27. J. B. Delos, Rev. Mod. Phys. 53, 287 (1981).

28. M. S. Huq, L. D. Doverspike, and R. L. Champion, Phys. Rev. A 27, 785 (1982).

29. R. C. Weast, editor, CRC Handbook of Chemistry and Physics, 65th edition (CRC Press, 1984), pD-215.

30. J. B. Taylor and I. Langmuir, Phys. Rev. 51, 753 (1937).

31. The heating wire used for the alkali oven is OMEGACLAD iron-constantan thermocouple wire (304-J-MO-062) manufactured by OMEGA Engineering, INC., which is metal-sheathed and contains magnesium oxide insulation.

32. A. M. Karo, M. A. Gardner, and J. R. Hiskes, J. Chem. Phys. 68, 1942 (1978).

33. R. E. Olson and B. Liu, J. Chem. Phys. 73, 2817 (1980).

34. F. W. Meyer, J. Phys. B 13, 3823 (1980).

35. V. N. Tuan and V. A. Esaulov, Phys. Rev. A 32, 883

(1985).

36. A. S. Schlachter, K. R. Stalder, and J. W. Stearns, Phys. Rev. A 22, 2494 (1980).

37. Yicheng Wang, R. C. Champion and L. D. Doverspike Phys. Rev. A 35, 1503 (1987).

38. B. H. Bransden and C. J. Joachain, Physics of Atoms and Molecules (Longman, 1983), p523.

39. A. R. Johnston and P. D. Burrow, J. Phys. B 15, L745 (1982).

40. A. L. Sinfailam and R. K. Nesbet, Phys. Rev. A 7, 1987 (1973).

41. A. Einstein, B. Podolsky and N. Rosen, Phys. Rev. 47, 777 (1935).

42. D. Bohm, Quantum Theory (Prentice-Hall, 1951), p611.

43. D. Bohm and Y. Aharonov, Phys. Rev. 108, 1070 (1957).

44. J. A. Wheeler and W. H. Zurek, Quantum Theory and Measurement (Princeton University Press, 1983).

45. J. S. Bell, Physics, 1, 195 (1964).

46. N. Herbert, Am. J. Phys. 43, 315 (1975).

47. J. F. Clauser and A. Shimony, Rep. Prog. Phys. 41, 1881 (1978).

48. F. M. Pipkin, Adv. At. Mol. Phys. 14, 281 (1978).

49. M. Lamehi-Rachti and W. Mittig, Phys. Rev. D. 14, 2543 (1976).

50. J. F. Clauser, M. A. Horne, A. Shimony and R. A. Holt, Phys. Rev. Let. 23, 880 (1969).

51. G. Herzberg, Molecular Spectra and Molecular Structure, 2nd edition (Van Nostrand Reinhold Co., New York, 1950) vol. I.

VITA

Yicheng Wang

Born on January 17, 1960 in Yiwu, Zhejiang, China. He graduated from Yiwu High School in 1975. He received B.S. degree in physics from Zhejiang University in 1982. He received M.S. degree in physics from the College of William and Mary in 1983.